Turbulent structure of the Arctic boundary layer in early summer driven by stability, wind shear and cloud top radiative cooling: ACLOUD airborne observations

Dmitry G. Chechin[1,4], Christof Lüpkes[2], Jörg Hartmann[2], André Ehrlich[3], and Manfred Wendisch[3]

[1]A.M. Obukhov Institute of Atmospheric Physics of the Russian Academy of Sciences, Moscow, Russia
[2]Alfred-Wegener-Institute, Helmholtz Centre for Polar and Marine Research, Bremerhaven, Germany
[3]Leipzig Institute for Meteorology, Leipzig University, Leipzig, Germany
[4]Moscow Center for Fundamental and Applied Mathematics, Moscow, Russia

Correspondence: Dmitry Chechin (chechin@ifaran.ru)

Abstract. Clouds are supposed to play an important role for the Arctic amplification process. This motivated a detailed investigation of cloud processes including radiative and turbulent fluxes. Data of the aircraft campaign ACLOUD were analyzed with a focus on the mean and turbulent structure of the cloudy boundary layer over the Fram Strait marginal sea ice zone in late spring/early summer 2017. Vertical profiles of turbulence moments are presented, which belong to contrasting atmospheric

5   boundary layers differing by the magnitude of wind speed, boundary-layer height, stability and by the strength of the cloud-top radiative cooling. Turbulence statistics up to third order moments are presented, which were obtained from horizontal level flights and from slanted profiles. It is shown that both of these flight patterns complement each other and form a data set that resolves the vertical structure of the ABL turbulence well. It is shown that especially during weak wind, even in shallow and relatively dry Arctic ABLs, cloud-top cooling can serve as a main source of turbulent kinetic energy. Well-mixed ABLs are

10   generated where TKE is increased and vertical velocity variance shows pronounced maxima in the cloud layer. Negative vertical velocity skewness points then to upside-down convection. Turbulent heat fluxes reach also maxima in the cloud layer as a result of cold downdrafts. Turbulent transport of heat flux and of temperature variance are both negative in the cloud layer suggesting an important role of large eddies caused by the cloud top cooling. In strong wind, wind shear is shaping the ABL turbulent structure, especially over rough sea ice. In the presence of mid-level clouds, cloud-top radiative cooling and thus also

15   TKE in the lowermost cloud layer are strongly reduced and the ABL turbulent structure becomes governed by stability, i.e., by the surface-air temperature difference and wind speed. In summary, the presented study documents vertical profiles of the ABL turbulence with a high resolution in a wide range of conditions. It can serve as a basis for turbulence closure evaluation and process studies in Arctic clouds.

1 Introduction

Within the past two decades an extraordinary climate change has been observed in the Arctic. Numerous processes and feedback mechanisms are discussed as possible reasons for the currently ongoing changes resulting in an enhanced Arctic warming compared to mid-latitudes, which is generally called the Arctic amplification. The effect of the processes and feedbacks have

5 well been documented by a large number of modelling and observational studies (e.g., Serreze and Francis, 2006; Graversen et al., 2008; Overland et al., 2011; Wendisch et al., 2017; Osborne et al., 2018). While the changes are obvious, the chain of interlinked processes and complex air-sea ice-ocean interactions leading, e.g., to reduced sea ice cover is not yet fully explored and quantified. A key factor in the framework of Arctic amplification feedbacks, which is in the center of this work, are clouds and their various effects. In early studies (e.g., Curry et al., 1996; Morrison et al., 2011; Shupe et al., 2011) it was found

10 that low-level mixed-phase stratocumulus clouds frequently occur over the Arctic and influence the surface heat budget and consequently the sea ice mass budget. In more recent investigations, clouds have been recognized to be involved in different feedback mechanisms accounting for the observed warming (e.g., Serreze and Francis, 2006; Pithan and Mauritsen, 2014; Goosse et al., 2018; Stapf et al., 2020). Changes of the cloud properties can occur due to several processes such as the increased advection of humid air masses (warm and humid air intrusions) over sea ice or due to the modified sea ice concentration and

15 its effect on fluxes of heat and humidity, (e.g. Tjernström et al., 2005). Here, we focus on the clouds' influence on components of the energy budget in the atmospheric boundary layer (ABL) relative to other impacts.

Although the crucial effects of Arctic clouds on the ABL energetics is widely accepted, a quantification, especially over sea ice covered regions is difficult since data are available from a limited number of campaigns only. The first analyses of the impact of Arctic clouds on the turbulent structure and on ABL energy fluxes using aircraft observations were presented

20 by Curry et al. (1988) and Finger and Wendling (1990). An improved understanding of the surface energy budget has been achieved by the Surface Heat and Energy Budget over the Arctic Ocean campaign (SHEBA, Uttal et al., 2002) and by the First International Satellite Cloud Climatology Project (ISCCP) the Regional Experiment Arctic Clouds Experiment (FIRE-ACE, Curry et al., 2000). Furthermore, process interactions and phase partitioning in the Arctic stratocumulus were studied using data from the Mixed-Phase Arctic Cloud Experiment (M-PACE) (Verlinde et al., 2007) and from the Indirect and Semi-Direct

25 Aerosol Campaign (ISDAC) (McFarquhar et al., 2011) over Alaska.

Important data on the entire cloudy ABL over sea ice has been obtained during the Arctic Summer Cloud Ocean Study (AS-COS, Shupe et al., 2013; Tjernström et al., 2014; Sedlar and Shupe, 2014; Sotiropoulou et al., 2014). By deriving the turbulent kinetic energy dissipation from surface based cloud radar it was shown that clouds often dominate the vertical distribution of turbulence in the ABL. The combination of the radar with sonic anemometer measurements on sea ice revealed that the turbu-

30 lent layer generated by clouds appears to be often decoupled from the near-surface layer (Brooks et al., 2017). Furthermore, these studies showed that in the presence of clouds, the strongest terrestrial cooling is shifted from the sea-ice surface to the cloud top. This promotes convective turbulent overturning within the cloud layer and the ABL is thicker and better mixed than in clear-sky conditions.

As a result, Arctic ABL clouds and the associated turbulent mixing may influence the lapse-rate feedback that was identified as one of the important drivers of Arctic Amplification (e.g., Pithan and Mauritsen, 2014). Moreover, turbulent mixing and entrainment affect the moisture budget and the life cycle of a stratocumulus layer, the magnitude of the cloud radiative forcing (e.g., Intrieri et al., 2002), as well as the air-mass transformation process during advection of moisture and heat into the Arctic

5   (Pithan et al., 2018). The frequency and intensity of the latter contributes strongly to the observed Arctic warming (e.g., Dahlke and Maturilli, 2017; Clark et al., 2021).

To summarize: Much insight into the turbulent and radiative processes, shaping the cloud-topped ABL in the inner Arctic, results from campaigns like SHEBA and ASCOS. Additionally, modelling studies (Solomon et al., 2011; Morrison et al., 2011; Solomon et al., 2014; Roesler et al., 2017) contributed to an improved understanding. However, only very few combined in

10   situ measurements of the vertical profiles of turbulent and radiative quantities are available from Arctic campaigns. Examples of airborne measured profiles were presented by Finger and Wendling (1990).

Such profiles are important to better understand the processes generating turbulence in the ABL and phenomena related to cloud turbulence and to its interaction with the surface. For example, turbulent coupling with the sea ice surface, especially in the presence of leads, supplies the cloud layer with moisture and cloud condensation nuclei. Turbulent entrainment at the

15   cloud top either serves as a source or a sink of moisture depending on the presence of a moisture inversion (e.g., Solomon et al., 2011; Egerer et al., 2021). Turbulent processes also modify microphysical cloud properties. Namely, the updraft branch of a large turbulent eddy causes condensation that leads to the growth of liquid water droplets and ice crystals (Morrison et al., 2012). Evaporation occurs in the downdraft branch of the eddy causing the cloud particles to shrink. Furthermore, liquid water droplets emit terrestrial radiation at cloud top which leads to cloud top radiative cooling and further intensification of

20   convective turbulence.

These turbulent and cloud microphysical subgridscale processes have to be parameterized for climate models. Parameterizations are often based on observations in lower latitudes and, thus, might be not appropriate for Arctic conditions. Indeed, models are known to have large difficulties to reproduce the Arctic mixed-phase clouds, especially, the longevity of the supercooled liquid water (Tjernström et al., 2008; Pithan et al., 2014). Therefore, one of the future major challenges is to further under-

25   stand the turbulence-microphysics-radiation interactions based on observations in the Arctic and to further develop appropriate parameterizations.

The goal of this paper is to describe and analyze the typical structure of the cloudy boundary layer in terms of turbulent and radiative energy quantities as found over sea ice and open ocean during the Arctic CLoud Observations Using airborne measurements during polar Day (ACLOUD) campaign (Wendisch et al., 2019). The ACLOUD campaign was carried out in

30   May-June 2017 over the Fram Strait marginal sea ice zone (MIZ) to the north-west from Svalbard. Unlike in most previous studies, we consider not only the more qualitative turbulence structure (as possible by surface based radar measurements) but quantify also the fluxes of momentum, heat and radiative energy as well as further turbulence quantities such as turbulent kinetic energy, variances and higher-order turbulence moments. Compared with Finger and Wendling (1990), a new aspect is to consider the variability due to the impact of external factors such as the mean wind field, sea ice cover and multi-layer clouds

35   and to obtain a better vertical resolution.

Our strategy is to investigate several contrasting cases with low-level clouds associated to the forcing mechanisms of turbulence and their variability. One of the important forcing parameters is the strength of mean wind, which varies from case to case due to a different synoptic situation. Second, the intensity of the cloud-top radiative cooling is strongly modulated by the presence of multi-layer clouds. Third, the surface roughness varies between smooth open water and relatively rough sea ice.

5 Another important factor is the wind direction over the marginal sea ice zone as it determines the near-surface stability and the direction of the near-surface heat flux (downward during on-ice flow or upward during off-ice flow). And finally, the ABL height and the cloud geometric thickness as well as cloud base differ from case to case. Although the ABL height is related to the ABL turbulence, it is often modulated by the large scale forcing, e.g., subsidence, or strength of the capping inversion.

The paper is structured as follows. We introduce the campaign and describe the measurement equipment in Section 2. Results

10 of different flights are presented and discussed in Section 3. A final discussion and conclusions follow in Section 4. Appendix A contains information concerning the accuracy of the measurements and Appendix B describes a diagnostic mixed layer model addressed in Section 3.

2 ACLOUD campaign

During the ACLOUD campaign the two research aircraft Polar 5 and Polar 6 (Wesche et al., 2016) of the German Alfred

15 Wegener Institute were used for collocated measurements in the cloudy and cloud free atmospheric boundary layer (ABL) over the open ocean and the marginal sea ice zone to the North and West of Svalbard. The general strategy was to use Polar 5 as a remote-sensing platform for cloud observations from above and Polar 6 for in situ measurements in clouds and below them (Wendisch et al., 2019). During some flights both aircraft were used for in situ observations.

ACLOUD took place during May/June 2017 covering the transition from late spring to early summer meteorological condi-

20 tions at the end of May (Knudsen et al., 2018). The last week of May 2017 was associated with northerly advection of cold air with a temperature of about -10 $°C$ over the sea ice-covered region north of Svalbard. Despite the relatively small temperature difference between the cold air mass and the open water surface satellite images still showed roll convection over the Fram Strait (Knudsen et al., 2018). During the first two weeks of June 2017 several episodes with warm air advection took place so that the air temperature increased over sea ice but it remained still below zero. The majority of flights above, in and below

25 low-level stratocumulus clouds over sea ice and open ocean were performed during this period.

During the ACLOUD period the research vessel (RV) Polarstern of Alfred Wegener Institute was drifting in the sea ice north of Svalbard (Wendisch et al., 2019). Some flights were carried out next to the ship but, e.g. safety rules did not allow parallel measurements in clouds with the tethered balloon (Egerer et al., 2019) which was operated next to the ship.

2.1 Aircraft instrumentation and data processing

30 The instrumentation of both aircraft including radiation and turbulence equipment is overviewed in Wendisch et al. (2019) and in Ehrlich et al. (2019). Here, we only summarize the relevant information about the instrumentation for turbulence and

boundary-layer observations. For measurement uncertainty we refer to Hartmann et al. (2018) and to further aspects described in Appendix A.

Both aircraft were equipped with identical meteorological instrumentation mounted at the nosebooms. It includes the Rosemount 858 five-hole probes, and two fast-response open-wire Pt100 temperature sensors in deiced and non-deiced Rosemount housings. Each aircraft was also instrumented with slow-response Vaisala temperature and humidity sensors (HMT-333) and also with static pressure sensors. Downward and upward shortwave and terrestrial longwave radiative energy fluxes were measured using Kipp and Zonen radiometers (CMP22 and CGR-4) installed at both aircraft.

The five-hole probe measures dynamic and static pressures and two differential pressures in orthogonal directions. Those data are used for the calculations of the true air speed, of the angle of attack α and the sideslip angle β of the aircraft. Both five-hole probes were equipped with effective deicing and purging systems for liquid water entering the pressure tubes in cloudy air. If not purged, the liquid water can cause serious problems, especially when it freezes in the tubes.

The measurements of position, movement, and attitude of the aircraft is based on an inertial navigation system (INS) are merged with the GPS signal. The data provide the aircraft roll, pitch, and yaw angles, ground speed and heading and vertical speed. These measurements yield the aircraft velocity vector relative to the Earth's fixed coordinate system. From the latter and the airflow vector provided by the 5-hole probe, the three components of the wind vector in geographic coordinates are calculated (e.g., Lenschow et al., 1986).

The majority of the ABL clouds observed during the campaign was dominated by liquid particles (Wendisch et al., 2019). Thus, only the liquid water content (LWC) is considered here as measured by a Nevzorov probe (Korolev et al., 1998) installed on Polar 6.

2.2 Flight patterns

Usually, horizontal flight sections are considered when turbulence moments are derived from high frequency aircraft measurements of meteorological variables. Turbulence statistics are calculated then by application of the eddy-covariance method. Different requirements exist for the length of horizontal flight sections. First of all, they should be long enough to keep the statistical sampling error small (Lenschow et al., 1980). Practically, the necessary flight length depends on the size of the relevant eddies, which in turn is a function, e.g. of the stratification and ABL height. The optimal length must consider also horizontal homogeneity and stationarity to separate mesoscale circulations along the track from turbulence. We found (see Appendix A) that the length of flight sections between 8 km and 18 km was sufficient to gain reliable vertical profiles of turbulence statistics. This result is based on both the statistical accuracy and the physically explainable structure of the obtained profiles of turbulence moments. Also the comparability of results of repeated flights with one or two aircraft at the same location was considered.

The difficulty of measuring the vertical flux profiles is that due to the range limitation of an aircraft only few flight levels are possible. Our strategy was to fly about 5-10 horizontal sections in staggered altitude levels (partly exactly upon each other, partly as a double-triangle pattern (Figures 1 and 2) as described also in Ehrlich et al. (2019). The aircraft range allowed us to sample profiles at 2-4 locations during one measurement flight.
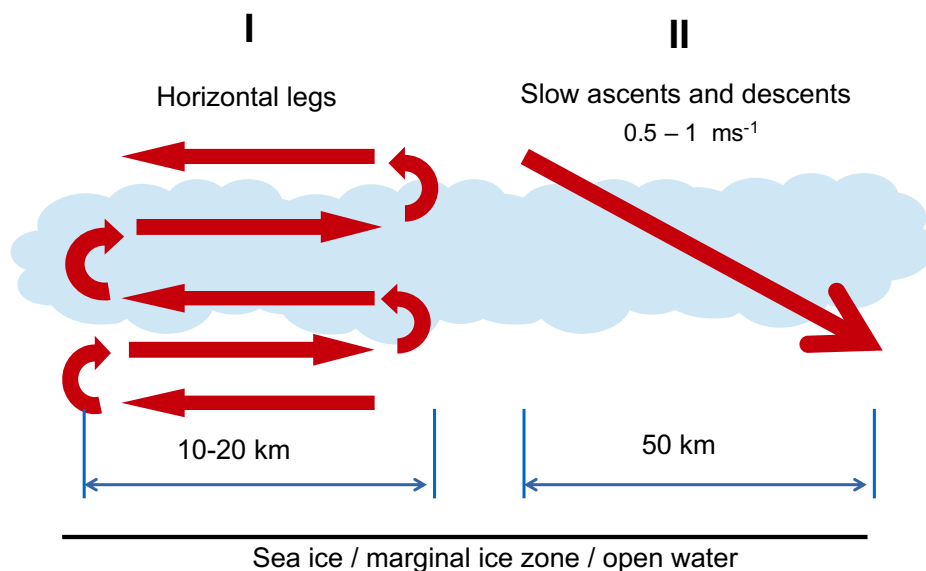
Figure 1. Flight pattern in clouds showing staggered horizontal legs and slanted profiles. Turns between legs were not included in the data analyses.

The drawback of these horizontal patterns is that the vertical resolution of a related flux profile is limited. For this reason we used also slanted profiles (see Figure 1) with low ascending and descending rates of about $0.5\,\mathrm{m\,s^{-1}}$ to $1.5\,\mathrm{m\,s^{-1}}$. This method has been used earlier by Mahrt (1985), Lenschow et al. (1988), Tjernström (1993), Aliabadi et al. (2016). Vertical sections were considered of about 100 m thickness corresponding to a flight distance of about 5-10 km. After applying moving averages, continuous vertical profiles were obtained. We expect that the accuracy of such profiles is smaller than that for horizontal flight sections due to a larger statistical error of the derived turbulence statistics at each height. Nevertheless, the information gained by this method is useful as shown by the comparison with results from horizontal sections.

As in Tetzlaff et al. (2015), who considered measurements over sea ice with sometimes also low values of heat fluxes, we show in Appendix A that the accuracy of the used turbulence probe was in horizontal legs sufficiently high to measure heat fluxes in the range of at least $5\,\mathrm{W\,m^{-2}}$. Also in Appendix A, specific uncertainties related with measurements in clouds are addressed. Comparison of the results of the two different aircraft and plausibility of obtained profiles point to even higher accuracy (see Figure 15 and its description).

3 Results

The main goal of our analysis is to discuss the variability of the cloud impact and to explain the differences between the observed cases. This will be done on the basis of mean variables but also of turbulent moments such as the vertical fluxes of

sensible heat H, and absolute values of momentum fluxes M with

$$H = \rho \, c_p \, \overline{w'\theta'} \tag{1}$$

and

$$M = \overline{\rho}\sqrt{\left(\overline{u'w'}^2 + \overline{v'w'}^2\right)} \,. \tag{2}$$

5 Furthermore, we consider the turbulent kinetic energy

$$TKE = \frac{1}{2}\left(\overline{u'^2} + \overline{v'^2} + \overline{w'^2}\right), \tag{3}$$

variances of velocity components

$$\sigma_u^2 = \overline{u'^2}, \quad \sigma_v^2 = \overline{v'^2}, \quad \sigma_w^2 = \overline{w'^2} \tag{4}$$

of potential temperature

10 $$\sigma_\theta^2 = \overline{\theta'^2} \tag{5}$$

the skewness of vertical velocity

$$S_w = \overline{w'^3}/\overline{w'^2}^{3/2}, \tag{6}$$

the vertical turbulent transport of sensible heat flux

$$T_{SH} = \overline{w'^2\theta'} \tag{7}$$

15 and the vertical transport of temperature variance

$$T_{TV} = \overline{w'\theta'^2} \,. \tag{8}$$

The description of cases starts with the effects of single-layer low clouds and ends with multi-layer clouds. A weak-wind single-layer case is described first in more detail, as it serves as a reference representing the turbulence structure when the cloud effect was clearly dominant.

20 **3.1   A single-layer cloud case with weak wind (5 June 2017)**

On 5 June, a single-layer stratocumulus deck was present over the sea ice to the north of Svalbard, which appeared to be almost transparent on the MODIS image (Figure 2). During the aircraft mission it could be seen visually that the layer of low clouds was rather solid. The region of observations was on the periphery of a high-pressure ridge with weak horizontal pressure gradients. This resulted in a weak south-westerly flow along the flight track in the lowest 500 m over the surface.

25   On the way north to RV Polarstern and back to south, P6 was performing slow ascents and descents (saw-tooth profiling), as shown by colored segments in Figure 2. Over Polarstern, P6 performed a double-triangle pattern with horizontal legs in
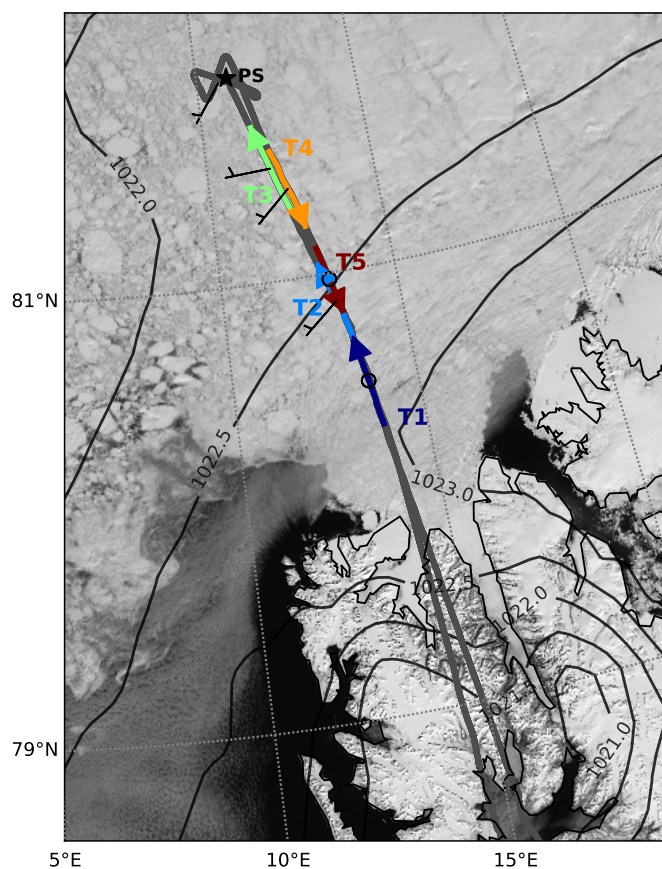
Figure 2. Polar 6 track on 5 June 2017 overlaid over the MODIS satellite image. T1-T5 represent descends and ascents of the aircraft and PS is the position of RV Polarstern. Wind barbs indicate the ABL averaged wind. The barbs are plotted for wind stronger than 2.5 knots, while weaker wind is indicated by an open circle. Isobars represent the mean sea level pressure field based on the ERA5 reanalysis (Hersbach et al., 2020).

different altitudes. Clearly, all profiles were obtained over sea ice but patches of open water (lead-like structures) were also observed.

In the following, results of horizontal flight legs over Polarstern and of slanted profiles along the track from T1 to the ship and back are discussed.

3.1.1 Mean ABL structure

Figure 3 shows vertical profiles of dynamic and thermodynamic parameters measured during profile patterns introduced in Figure 1. In this way, the mean vertical ABL structure of the cloud-topped mixed layer is illustrated as obtained from the saw-tooth profiling and also during the horizontal legs at different heights over Polarstern. The boundary layer profiles document similarities at the different positions but also certain variability. The main characteristics were a shallow boundary layer with potential temperatures about 5 K below the freezing point, weak wind with a horizontal speed of $1 \ \mathrm{m \, s^{-1}}$ to $2 \ \mathrm{m \, s^{-1}}$ and a shallow cloud layer with top at 400 to 500 m height. In the southern profiles (profiles T1 and T5 in Fig. 3b), a low-level jet was present above the mixed-layer. Vertical profiles of wind direction (Fig. 3c) show that wind appeared rather uniform in the cloud layer, while a step change in direction below the cloud base is clearly visible in several profiles, especially at T4 and T5. This hints to a decoupling between the well-mixed cloud layer and the surface-based boundary layer in some profiles. At the same time, the potential temperature and specific humidity profiles show no signs of decoupling.

All profiles of potential temperature indicate that the ABL was well mixed and capped by a sharp temperature inversion (Fig. 3a). The increase of temperature in the capping inversion varied between about 5 K at position T4 and smaller values at T1 and T5. Also, at T1 and T5 the inversions were smoother than at other positions. A strong jump at the cloud top was also found for the relative humidity (Fig. 3d) whose values decreased rapidly and also the mixing ratio decreased, although less pronounced. Small maxima are visible in the mixing ratio (Fig. 3e) right above the cloud top within the capping inversion. This phenomenon is best seen at T1, but also at T5 and is weakly present at T2. A similar, yet stronger maximum of the mixing ratio was also found in the measurements performed on the same day using a tethered balloon at the PS location Egerer et al. (2021).

The ABL variability along the considered track was most obvious in the LWC profiles (Fig. 3f) as measured by the Nevzorov probe, which shows that the cloud layer was thickest (300 m) and contained the most liquid water at position T1. There, the cloud base was near the lowest flight altitude (about 100 m). Further north, the cloud layer first became thinner in profiles T2 and T3 and the cloud top raised to about 540 m. Over Polarstern, the cloud layer became thicker again, while the cloud top lowered to 400 m. As it is typical for a well-mixed stratocumulus layer, the LWC was increasing almost linearly with height with the same slope in all profiles. This was confirmed also by the results of the averaged horizontal flight legs.

3.1.2 Turbulent structure

It is well-known that the main driver of turbulence in single-layer stratocumulus is the cloud-top radiative cooling. In the case investigated here a strong cloud-top cooling was present in all profiles (Figure 4b). The jump of the net terrestrial energy flux LW_{net} across the cloud-top layer was in the range of -50 to -70 $\mathrm{W \, m^{-2}}$ (Figure 4a). We assume here that LW_{net} is positive
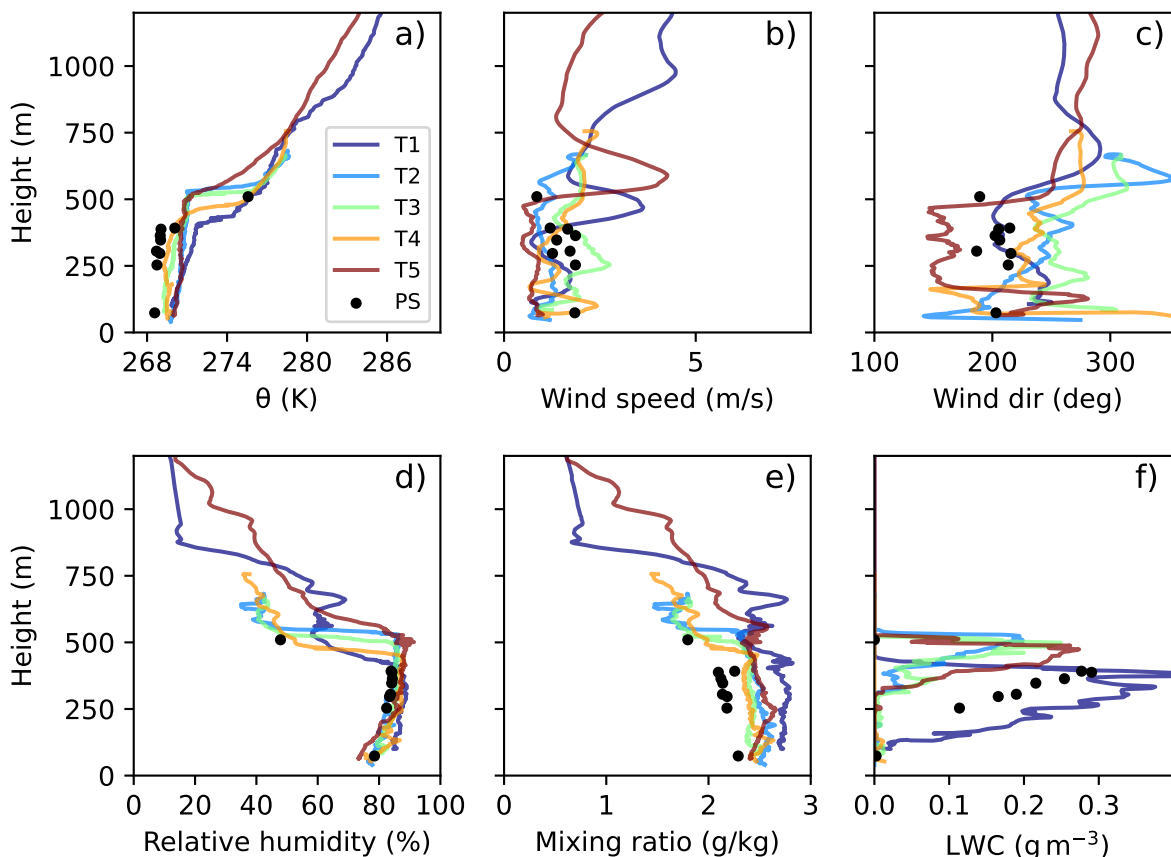
Figure 3. Vertical profiles of the mean potential temperature, wind speed and direction, absolute and specific humidity and the liquid water content obtained during slant ascents and descents of P6 on its way to Polarstern and back on 5 June 2017. The locations of the ascents and descents are shown in Figure 2.

upward. The impact of the radiative cloud top cooling will be discussed based on the profiles of turbulence moments. Some of these moments, derived from the horizontal legs over RV Polarstern, were shown already in Wendisch et al. (2019), their Figure 18. Here, we extend this analysis and consider both results of horizontal legs at PS and of the slanted profiles (Figure 5).

5   The cloud impact on several turbulence moments is obvious. Values of turbulent heat flux H were clearly elevated in the cloud (Fig. 5a). Thus, the profiles of H deviated from a shape typical for quasi-stationary convective ABLs developing over a heated surface where H decreases linearly with height. The values within the cloud layer reached to about 12 W m^{-2} for H and decreased to about 5 W m^{-2} over RV Polarstern or became close to zero for slanted profiles. Obviously, positive heat flux was generated by the cold downdrafts (due to cloud-top cooling) and warm updrafts. At the cloud top, one would expect a
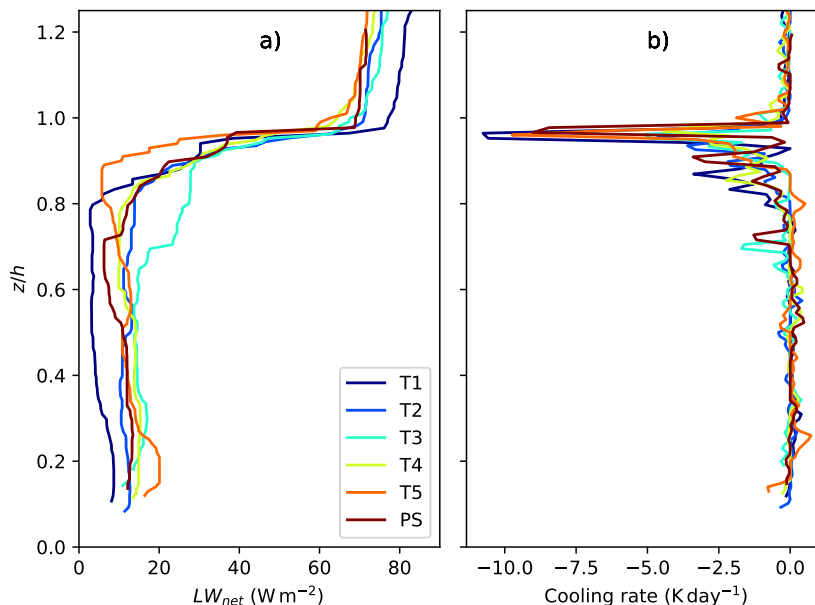
Figure 4. Vertical profiles of the net terrestrial radiative energy flux LW_{net} and of the cooling rate associated with the vertical divergence of LW_{net} as observed during saw-tooth profiling by Polar 6 on 5 June 2017. The altitude is normalized by the cloud top height h so that individual profiles can be compared.

significant negative heat flux due to entrainment considering the presence of a temperature jump across the inversion. Indeed, the measured value of H was about -3 W m^{-2} to -4 W m^{-2} and thus the flux was downward.

The momentum flux M had a clear maximum next to the cloud bottom of about 0.5 kg m^{-1}s^{-2} (Fig. 5b). Another maximum was found close to the cloud top, but only in the profile obtained from horizontal flight sections. The latter maximum was most

5 probably associated with the entrainment flux of momentum.

The positive heat flux within the cloud layer as a consequence of the radiative cooling at cloud top was responsible for the TKE generation in the cloud as well as for the maximum in σ_w^2 (Fig. 5d,f) in the upper portion of the mixed-layer. Nevertheless, TKE was almost height constant (Fig. 5f) and did not show a clear maximum in the center of the ABL as visible in σ_w^2 (Fig. 5d). Probably, this is due to high values of TKE and variances of horizontal wind components in the subcloud

10 layer associated with wind shear caused by the surface roughness and also thermal inhomogeneities. The profiles of σ_w^2 and of σ_u^2 and σ_v^2 (Fig. 5d,e) were similar to those found for a stratocumulus-topped ABL by Nicholls (1984) and Nicholls (1989) based on aircraft observations over the North Sea and by Moeng (1986) based on large-eddy simulations. Such a structure is also typical for a dry convective ABL heated from below. The difference is that there, the maximum of σ_w^2 appears in the lower portion of the ABL (Lenschow et al., 1980), while in our case, it was located in the middle or even in the upper part.

15 Another evidence of the upside-down convection was the negative skewness S_w of vertical velocity throughout the cloud layer Fig. 5g). Close to the cloud top, S_w was close to zero. Such a structure of S_w in the Arctic stratocumulus was reported
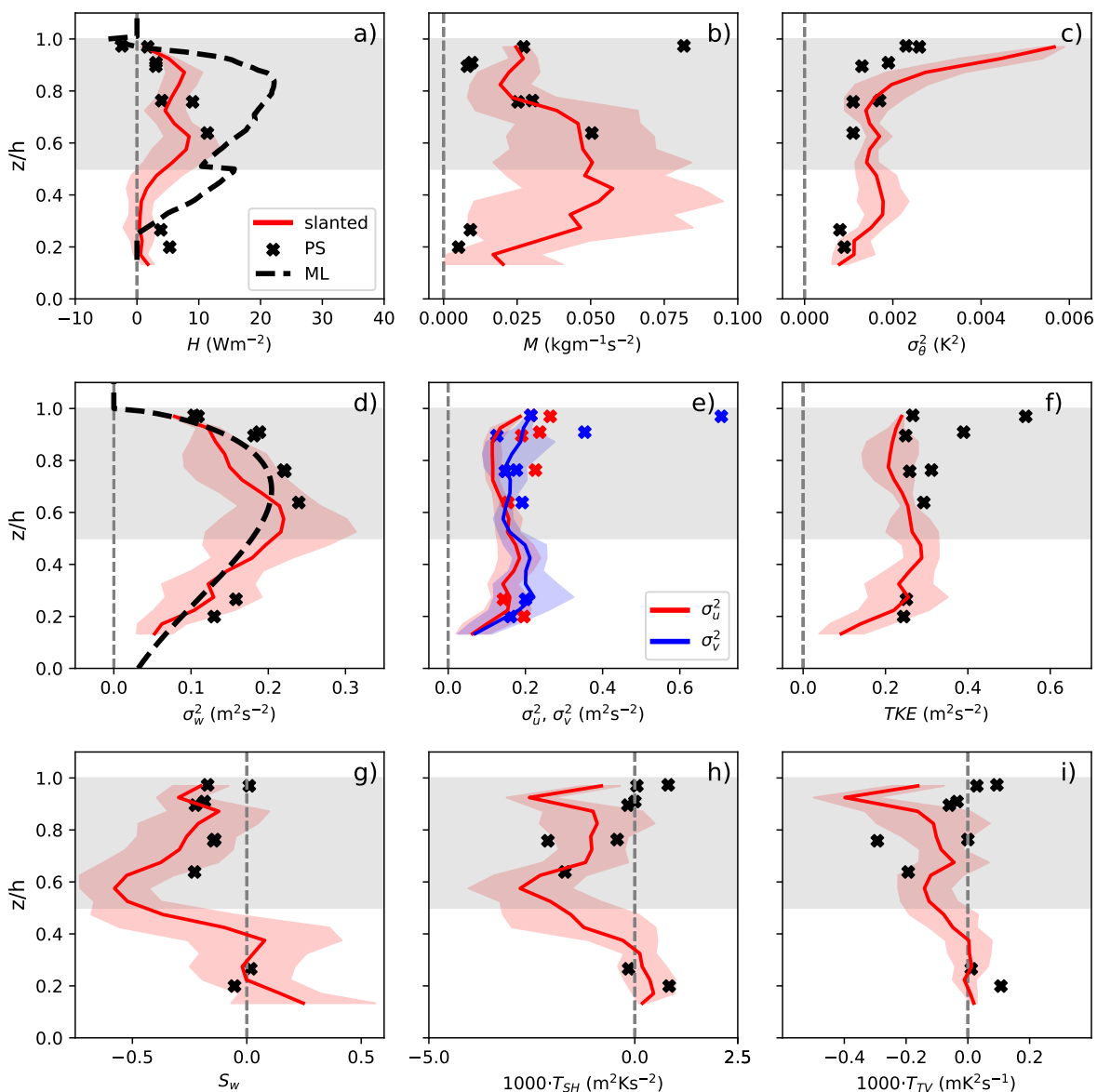
Figure 5. Vertical profiles of turbulence statistics obtained from horizontal legs over RV Polarstern (black crosses) and slanted profiles on 5 June 2017. Red lines represent mean values based on four slanted profiles, while red shading indicates ± one standard deviation. The cloud layer as observed over the RV Polarstern is shown with grey shading. The black dashed line in (a) shows the results of the diagnostic mixed-layer model with the entrainment flux prescribed from Eqs. (B11) and (B13) and in (d) - the Lenschow parameterization for σ_w^2 given by Eq. (12).

earlier by Sedlar and Shupe (2014), as well as by Hogan et al. (2009) based on radar and lidar data. In the subcloud layer, a sharp transition of S_w to zero or positive values is observed. This might represent a transition from the upside-down convection in the cloud layer to the turbulence generated by shear or slight heating from the surface.

It is also important to consider the turbulent transport of heat flux T_{SH} (Fig. 5h). In nonlocal turbulence closure schemes this
5 term is seen as the origin of the nonlocal, sometimes also called "countergradient", transport by large eddies (e.g. Zilitinkevich et al., 1999). We see here again a structure pointing to upside down forcing, namely negative downward transport in the cloud layer but slight upward transport near the surface.

Another third moment, namely, the transport of temperature variance T_{TV} (Fig. 5i), is also associated with nonlocal transport by large eddies. In the considered case, T_{TV} had a similar vertical structure as T_{SH} with negative values in the cloud layer. It
10 should be noted that only two horizontal flight segments show significant negative values of T_{SH} and T_{TV} in the cloud layer. However, vertical profiles of T_{SH} and T_{TV} based on slanted profiles provide a clear evidence of negative T_{SH} and T_{TV} in the cloud.

Figure 5c also shows an increased temperature variance close to the ABL top. This is typical for convective and cloud-topped ABLs and is related to the entrainment of air from the inversion layer with strong temperature gradient (Nicholls, 1984,
15 1989). Young (1988) found that one of the reasons for the increasing variance of θ at the top of a strong convective ABL is the forcing by the vertical gradient of temperature rather than turbulent transport of the temperature variance through the capping inversion. This is confirmed here since at the cloud top T_{TV} is near zero. But undulating cloud top, as well as gravity waves in the stably stratified inversion layer contribute also to an increased temperature variance near the capping inversion.

3.2 A single-layer cloud case with strong wind (2 June 2017)

20 Another single-layer stratocumulus case observed during ACLOUD on 2 June represents a flow directed almost parallel to the MIZ but with a slight on-ice flow component. It differs from the 5 June case by a stronger wind and stronger horizontal gradients of the ABL height and temperature. On that day, Polar 6 performed saw-tooth profiling over open water and sea ice on the way north and a double-triangle pattern in the cloud-topped boundary layer over sea ice at the northern end of the track (Fig. 6).

25 Figure 7 shows vertical profiles of mean variables as observed during the saw-tooth ascents and descents. Clearly, a thick mixed layer was present over the open water up to about 750-800 m height (profiles T1, T2 and T3). The ABL height gradually decreased along the south-north flight track and reached about 350-400 m in the northernmost profiles T6 and T7. The cloud layer thickness also decreased from 500 m in the southern profiles to 250-300 m in the northern profiles (Fig. 7f). A strong capping inversion was observed over both open water and sea ice. The magnitude of the temperature jump at the cloud top
30 reached 5 K to 7 K (Fig. 7a). A much drier air was lying over the ABL and the jump-like decrease of the mixing ratio amounted to about 2 g kg^{-1} across the cloud top (Fig. 7e). A low-level jet was present in all wind profiles (Fig. 7b). Its magnitude was strongest over sea ice (profiles T5 and T6) where it reached about 14 m s^{-1}.
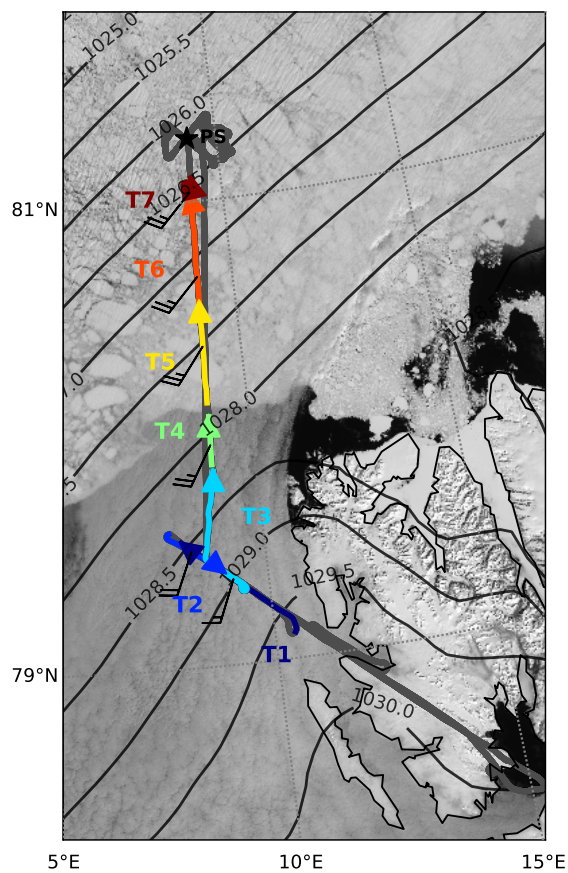
Figure 6. Polar 6 flight track on 2 June 2017 overlaid on the MODIS satellite image. T1-T7 represent descends and ascents of the aircraft. The wind barbs are showing the wind speed and direction averaged over the profile segments within the ABL. Isobars represent the mean sea level pressure field based on the ERA5 reanalysis.
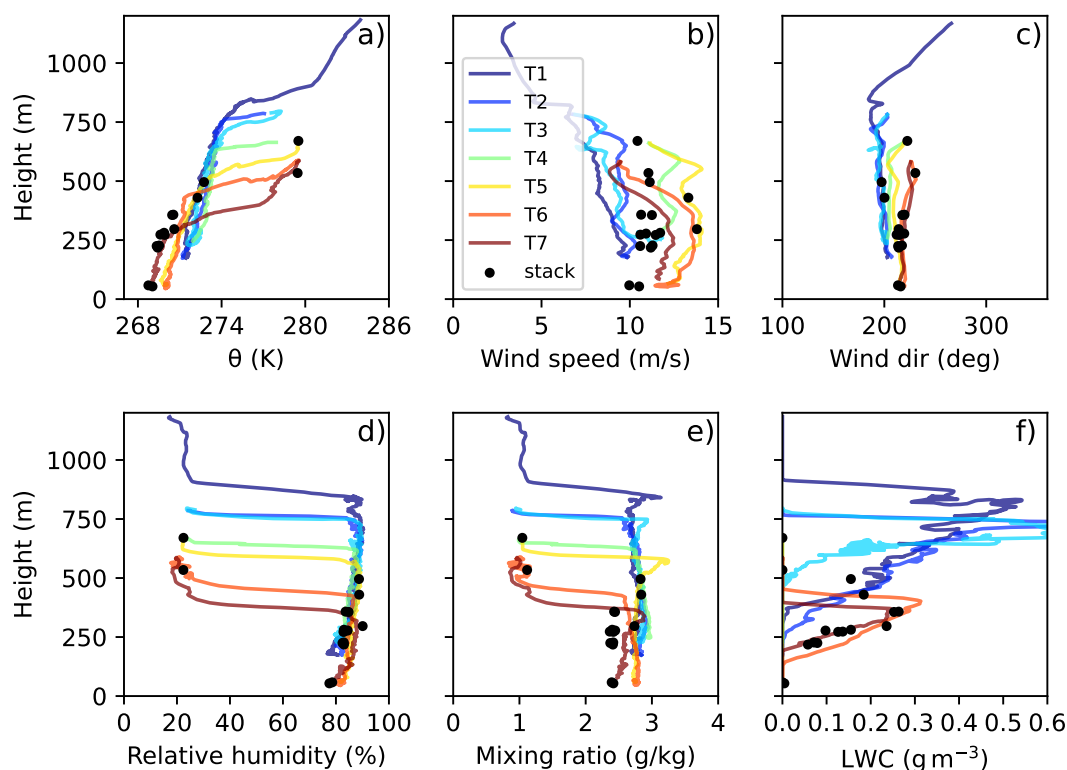
Figure 7. Vertical profiles of the mean potential temperature, wind speed and direction, absolute and specific humidity and the liquid water content obtained during slant ascents and descents of P6 on its to Polarstern and back mageon 2 June 2017. The locations of the ascents and descents are shown in Figure 6.

The main reason for such a South-North variability might have been that the ABL wind was not directed along the flight track, but from southwest (220 degree). Thus air parcels that arrived at positions T6 and T7 were influenced by sea ice in the MIZ while T1-T3 rather represent open ocean conditions.

The occurrence of the observed low-level jet might have synoptic origins but also might have to do with the mesoscale thermal structure of the lower atmosphere. Low-level jets and breeze-like circulations are common over the MIZ (e.g. Chechin et al., 2013; Chechin and Lüpkes, 2017) and are influenced by the horizontal temperature gradient in the ABL and the sloping inversion at the ABL top. The latter was especially strong in this case.

Similar to the 5 June case, a strong cloud-top terrestrial radiative cooling was present on 2 June both over open water and sea ice. The cooling rates were similar with about -9 K h^{-1} maximum cooling for all profiles independent if over sea ice or open water (not shown here, see Fig. 16 in Wendisch et al. (2019)). The cooling explains some of the observed characteristics of the turbulent structure. However, the latter differed on 2 June over sea ice from that on 5 June. This becomes clear from

a comparison of the results from slanted profiles shown in Figure 5 with those in Figure 8 (Profiles T5 and T6). The main difference is the occurrence of a pronounced TKE maximum in the lower portion of the ABL on 2 June, which does not exist on 5 June. It is clearly related to the maxima of σ_u^2 and σ_v^2 and not to the maximum of σ_w^2. Near the surface, the absolute values of σ_u^2 and σ_v^2 reach 0.6 and 0.8 m^{2}s^{-2} (during profile flights), respectively, which is two to three times larger than the largest value of σ_w. On 5 June, σ_u^2 and σ_v^2 are much smaller and contrary to 2 June σ_w^2 has a pronounced maximum in the upper portion of the ABL and thus in the cloud. Although the vertical resolution obtained by the horizontal legs is not high enough on 2 June to resolve the lower maximum, these measurements do not contradict the profile flights (Figure 8). σ_w shows in the cloud layer values, which are at least elevated relative to the value obtained by the lowest horizontal leg on 2 June. This hints to two sources of turbulence: one in the cloud layer and the second one close to the ground.

Obviously, the increase of TKE in the lower part of the ABL can be attributed to the dominant role of the TKE production by wind shear, given that a strong low-level jet was present in profiles T5 and T6. One can conclude that the overall buoyancy production of TKE was relatively small. Small positive values of sensible heat flux occurred in the cloud layer, but in the lower part of the ABL we detected negative heat flux. The latter was due to the warm air advection over colder sea ice. Thus, the ABL was being cooled both at its top and bottom. The cooling at the ABL top produced negative vertical velocity skewness S_w close to the top. In the middle of the ABL, we observed a pronounced shift to positive values of S_w indicating surface generated turbulence. We conclude that the surface was shaping the turbulence structure but slight cloud-generated turbulence was still present, although it did not govern the entire ABL turbulent structure.

In contrast, in the thicker ABL over open water the turbulence generation due to cloud-top cooling was evident, as can be seen in the turbulence statistics obtained during the T1 and T2 descent and ascent shown in Figure 9. There was a well-defined region of positive sensible heat flux in the upper part of the cloud layer with values up to 20 W m^{-2} (Fig. 9a). The values of σ_w^2 and TKE also had maxima in the upper part of the cloud layer (Fig. 9b,c). There, S_w was mostly negative (Fig. 9d) also indicating a strong cloud-top forcing.

To summarize, a stronger wind and a rather shallow ABL over sea ice produced a turbulent ABL structure, where the effect of wind shear on turbulence statistics was evident even in the presence of a cloud layer and cloud-top radiative cooling. Wind shear was associated with high surface drag. Over open water, cloud-top radiative cooling was of the same magnitude as over sea ice. Despite that, a thicker ABL, as well as a thicker cloud layer resulted on 2 June over open water in a different turbulent structure of the cloud layer than over sea ice, which was governed over open water by cloud-top radiative cooling and not by wind shear as over sea ice.

Also, it should be noted that roll-like cloud structures are clearly seen over the MIZ in the MODIS satellite image for 2 June (Fig. 6). The signature of those structures was also found in the aircraft observations during horizontal legs of the double-triangle pattern. Namely, the wave-like structures were clearly seen in the liquid water content, air temperature and wind speed components (not shown here). A detailed description of the characteristics of such structures as well as of their role in turbulent exchange is out of the scope of this paper.
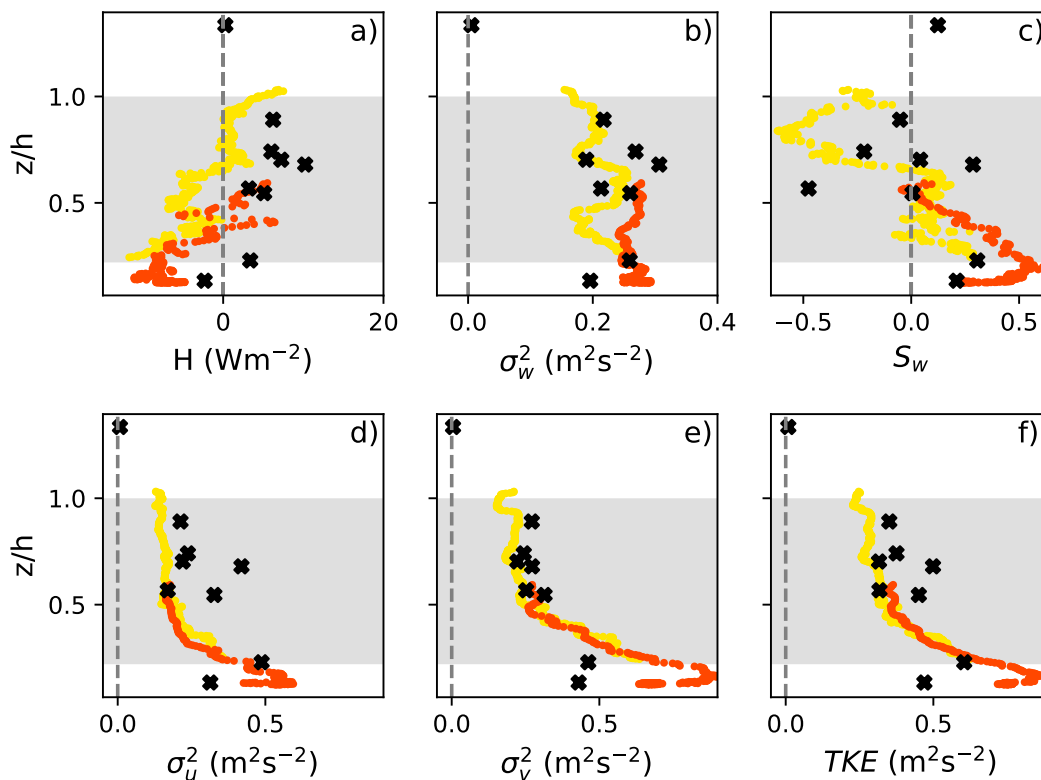
Figure 8. Vertical profiles of turbulent sensible heat flux H, vertical velocity variance σ_w^2 and skewness S_w, horizontal velocity components variances σ_u^2 and σ_v^2 and turbulent kinetic energy TKE as observed over sea ice on 02 June 2017 based on horizontal flight sections (black crosses) and slanted profiles T5 and T6. The colors of T5 and T6 are the same as in Figures 7 and 6.

3.3 Multi-layer cloud cases

Based on data from a cloud radar installed on sea ice, Shupe et al. (2013) showed that a secondary mid-level cloud layer may reduce the radiative cooling at the top of the lower cloud layer. This leads to a reduction of the generation of turbulence at the lower-layer cloud top as compared with a single-layer cloud. We show in the following that the aircraft observations confirm
5   the finding of Shupe et al. (2013). The latter is based, however, mainly on the study of σ_w^2 statistics only because further turbulence moments cannot be derived from radar. Thus, our study adds further aspects to the understanding of the impact of multi-layer clouds on the lower atmosphere.

3.3.1 A two-layer cloud case with a slightly convective boundary layer (14 June 2017)

We start with results from 14 June obtained north of Svalbard where the estimated sea ice fraction was about 90-95 % based on
10   visual observations (Figure 10). The air advected from North was only slightly colder than the average surface temperature of
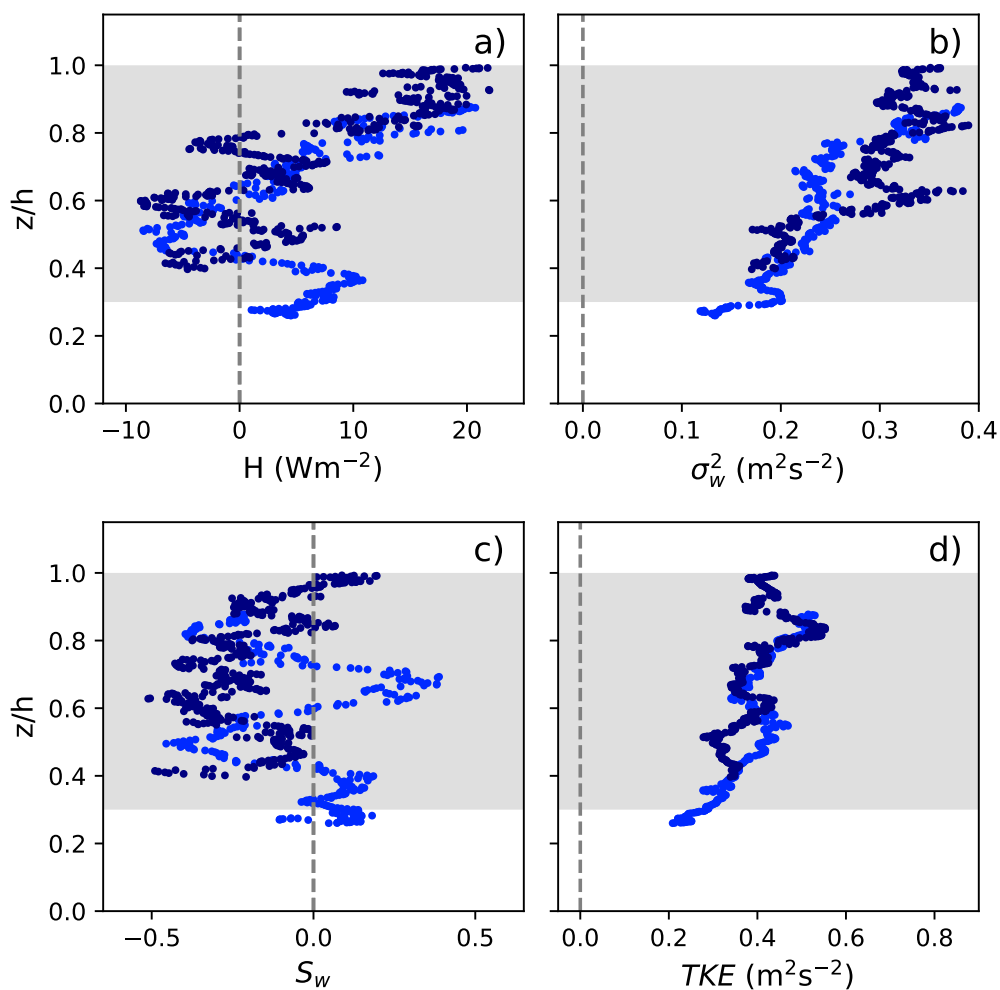
Figure 9. Vertical profiles of turbulent sensible heat flux H, vertical velocity variance σ_w^2 and skewness S_w and turbulent kinetic energy TKE as observed over open water on 02 June 2017. Colors of the profiles T1 and T2 are the same as in Figures 7 and 6.
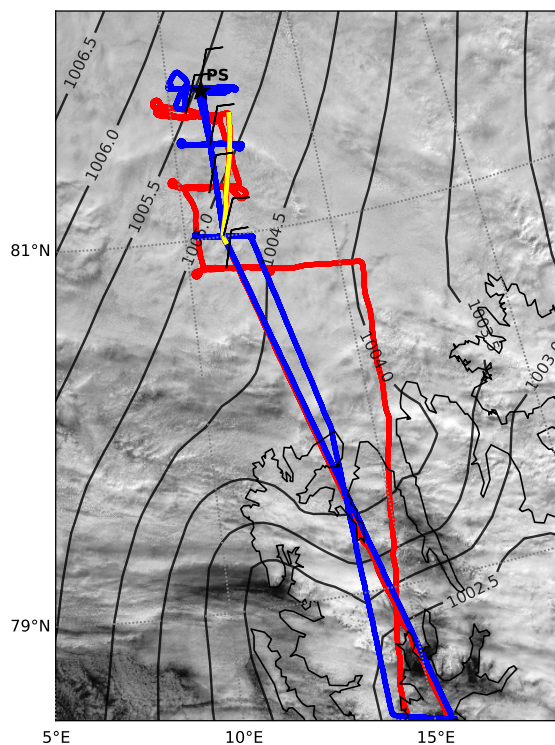
Figure 10. Tracks of Polar 5 (blue) and Polar 6 (red) on 14 June 2017 overlaid over MODIS satellite images. The wind barbs are showing the wind speed and direction averaged over the profile segments within the ABL. Only the northernmost cross wind leg nof Polar 6 and the two northermost two cross wind legs of Polar 5 are analyzed. The yellow line marks the descend of Polar 6 used for the analysis.

the mixture of ice and water in leads and small polynyas. But this temperature difference was high enough for the development of a slightly convective ABL in the lowermost 400 m. In contrast to the profiles shown in the previous sections, a mid-level cloud layer existed with base at about 1900 m and top at 2400 m (see LWC in Figure 11b). This cloud layer produced strong cloud top radiative cooling as can be concluded from LW_{net} indicating a strong vertical divergence at cloud top (Fig. 11c).

5 There, the maximal cloud top cooling rate amounted to about -11 K h^{-1}. In contrast, the lower cloud layer could not produce a pronounced cloud top cooling because the loss of terrestrial radiation was compensated by the emission of the cloud base of the second cloud layer above. This is obvious in the low vertical divergence of LW_{net}, which was much less pronounced at the top of the lower cloud layer at about 400 m and resulted in about -1 K h^{-1} cooling rate. The profiles of sensible heat flux (Fig.
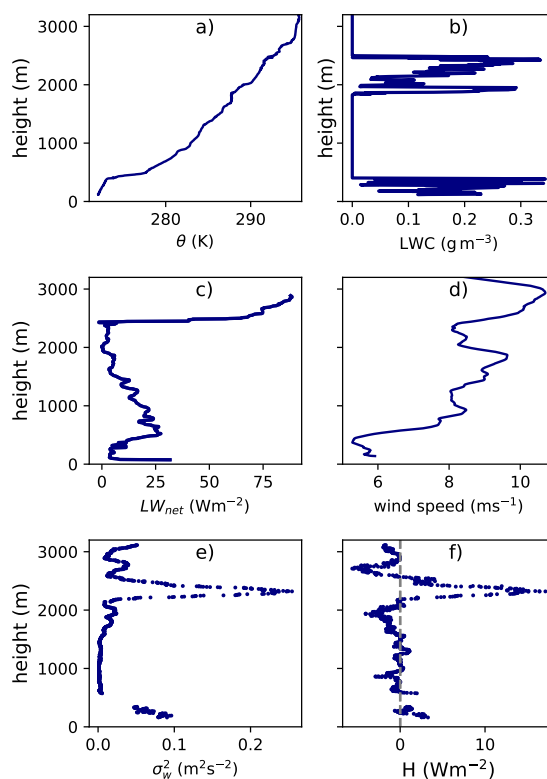
Figure 11. Results for 14 June 2017 obtained from a descent of Polar 6 in between the locations of the northernmost horizontal legs and the middle ones shown in Figure 10.

11f) and of the vertical velocity variance (Fig. 11e), both estimated from a descent of Polar 6 near the northern end of the flight pattern (yellow flight segment in Fig. 10), indicate much stronger mixing in the upper cloud than in the lower cloud.

Concerning results of the horizontal flight sections, we concentrate here only on the three northernmost cross-wind legs (Figure 12). The reason is that in this region the surface and cloud conditions showed less variability between and along the different horizontal sections. Also, there were icing problems along the southern legs.

Apparently, a well-mixed layer had developed below cloud top. In the ABL, heat fluxes were directed upward and show a more or less linear decrease with height from values of about 10 W m^{-2} at $z = 0.2h$ to 0 W m^{-2} at cloud top ($z = h$). This led to negative values of the bulk Richardson numbers Ri_b where gradients of temperatures and wind entering Ri_b refer to the two lowermost legs. Values are $Ri_b = -0.07$, $Ri_b = -0.05$, and $Ri_b = -0.20$ from South to North (or $z/L = -0.34$, -0.96 and -0.81 respectively where z is the altitude of the lowest horizontal flight leg and L is the Obukhov length).

Since the external conditions (temperature, wind, ABL top, cloud thickness) did not change significantly between the locations of the flight legs, it is expected that the turbulent quantities varied also very little. And indeed, despite the small signals, the accuracy of both aircraft data is obviously high enough to show very similar results at the different locations (Figure 12).
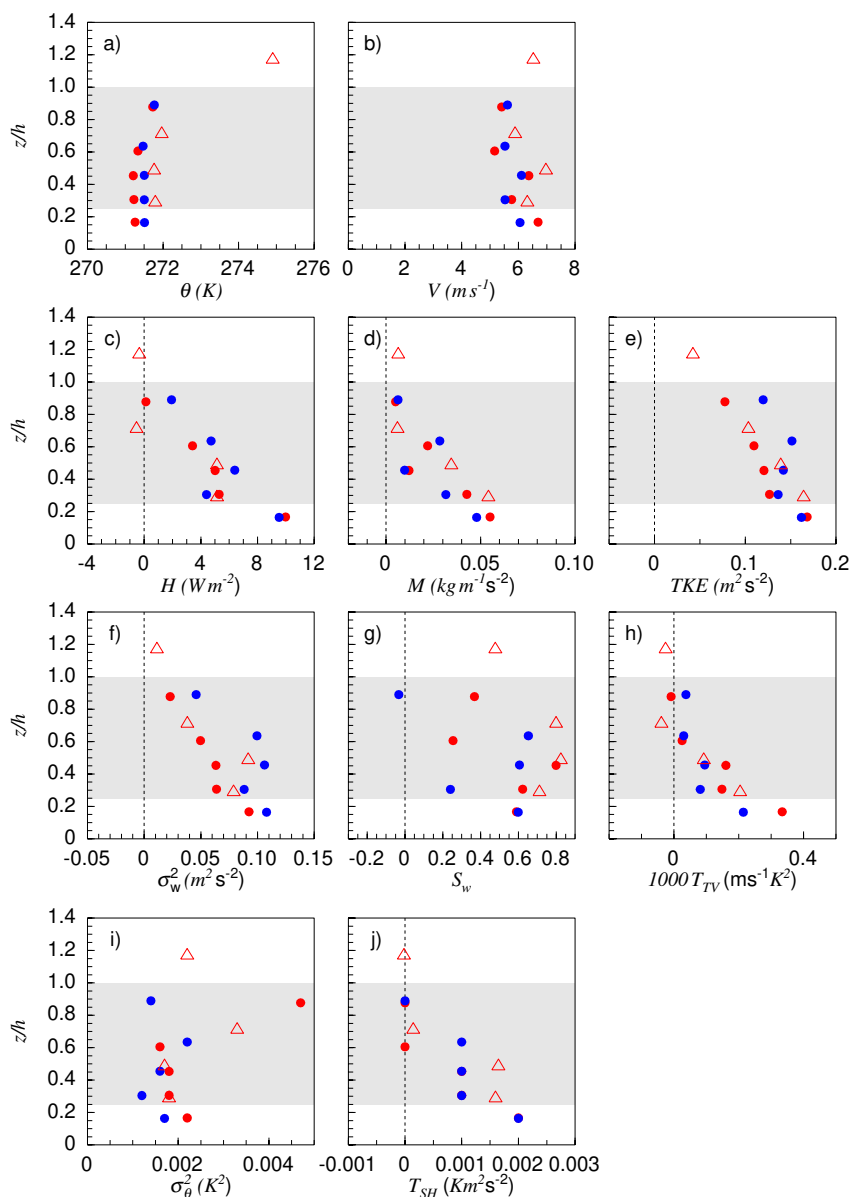
Figure 12. Turbulence statistics based on horizontal flight legs of 14 June 2017 obtained from Polar 5 (closed symbols) and Polar 6 (open symbols). Results of Polar 5 refer to the two northernmost blue legs shown in Figure 10. The Polar 6 result on 14 June refer to its northernmost flight leg (red in Figure 10). Altitude is normalized by the cloud top height $h = 400$ m.
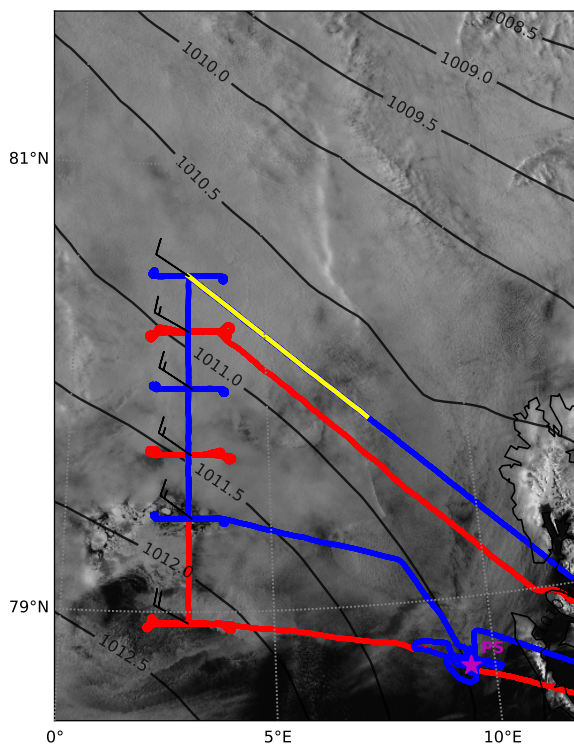
Figure 13. Tracks of Polar 5 (blue) and Polar 6 (red) on 20 June 2017 overlaid over the corresponding MODIS image. The yellow line refers to the Polar 5 descend shown in Figure 14.

It is especially interesting to compare this case with the case observed on 5 June (see Figure 5). There are the following differences: First, on 14 June neither heat flux nor variance of vertical velocity had a distinct maximum in the cloud as on 5 June. Moreover, the absolute values of σ_w^2 and of TKE were almost twice as small on 14 June despite stronger wind and positive surface heat flux. Another difference is that on 14 June the vertical transport of heat flux T_{SH}, and of temperature variance T_{TV} and also S_w remain positive in the entire ABL (except near the capping inversion). This indicates that the processes are not cloud-top driven but surface driven. The reason for this different behavior is clearly the existence of the mid-level clouds, which leads to a reduction of the cloud top cooling and thus suppressed mixing at the cloud top.
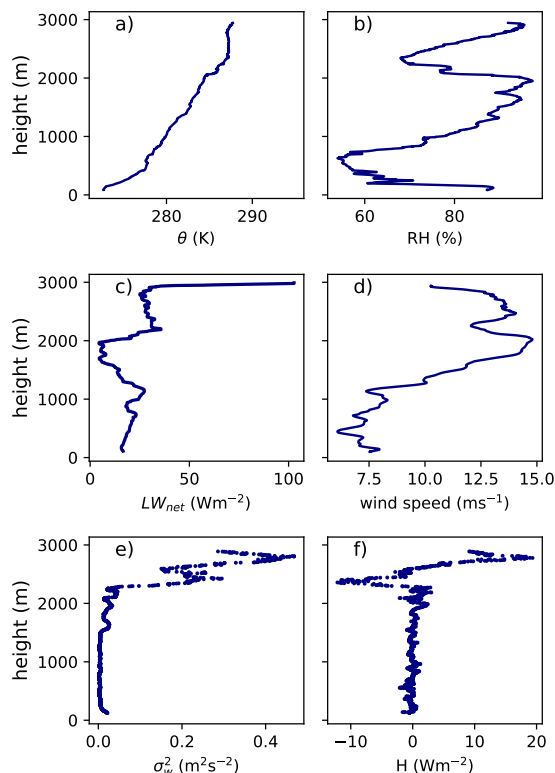
Figure 14. Results for 20 June 2017 obtained from a descent of Polar 5 at the location of the northernmost horizontal legs (see Figure 13).

3.3.2 A three-layer cloud case with a stable boundary layer (20 June 2017)

On 20 June, again a multi-layer cloud system has been observed in westerly wind conditions and over a region with an ice fraction of about 95 %. Figure 14 shows vertical profiles obtained during a descent of Polar 5 in the northern part of the observational area. No Nevzorov probe was installed on Polar 5, but visual observations and the vertical profile of relative humidity (Fig. 14b) allowed one to detect even three cloud layers with cloud tops at about 350 m, 2100 m, and 3000 m. The strongest cooling occurred at the uppermost cloud top (Fig. 14c) where the maximal cooling rate reached -10 K h^{-1}. Below that cloud top, also the strongest turbulence was observed as can be seen from σ_w^2 and H profiles (Fig. 14e,f) having maxima of about 0.47 m^{2}s^{-2} and 19 Wm^{-2}, respectively. Across the cloud top at 2100 m, radiative cooling amounted to about -1.5 K h^{-1} which resulted in much weaker, yet non-zero values of σ_w^2 and H of about 0.03 m^{2}s^{-2} and 2.5 Wm^{-2}.

Figure 15 shows results for the lowest cloud layer and indicates a fundamental difference between the ABLs observed on this day and on 14 June. On 20 June, the westerly winds led to a near-surface stable stratification ($Ri_b = 0.16$ and $Ri_b = 0.27$ or $z/L = 0.29$ and $z/L = 0.56$, respectively for the Polar 5 legs at the lowest heights). This caused downward but very small absolute values of fluxes of sensible heat. These numbers are probably at the detection limit, nevertheless, the good qualitative
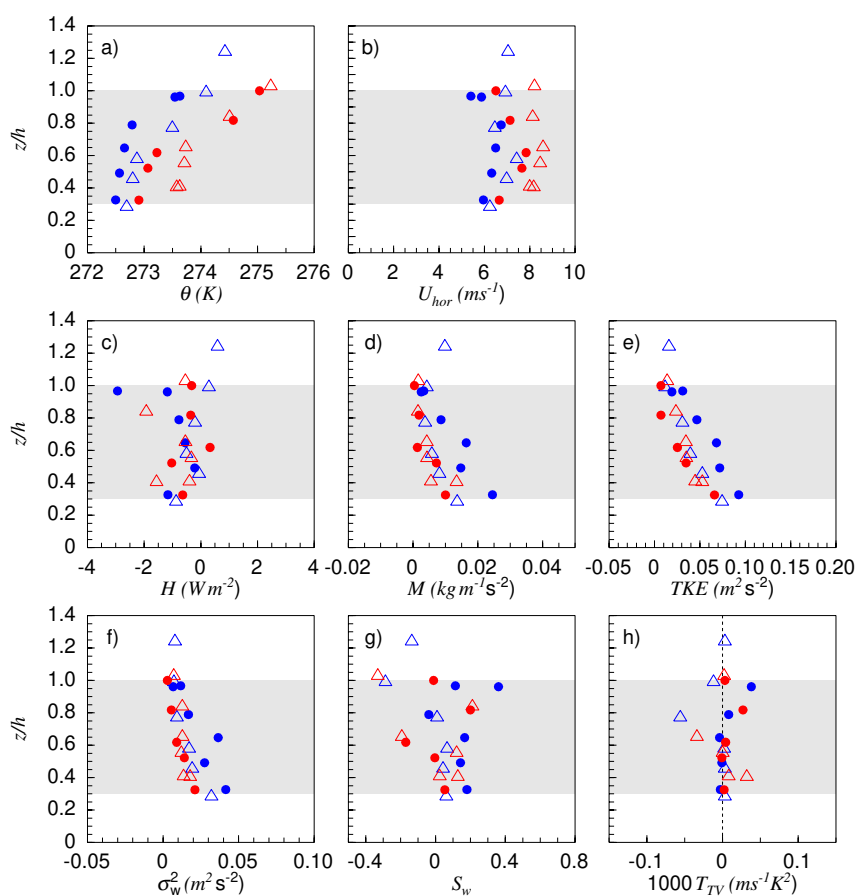
Figure 15. Turbulence statistics for the lowermost cloud layer based on horizontal flight legs of 20 June 2017 obtained from Polar 5 (blue symbols) and Polar 6 (red symbols). The results refer to the two blue and red northernmost flight legs of the aircraft (see Figure 13). Closed (open) symbols refer to the northern (southern) positions. Altitude is normalized by the cloud top height, for Polar 5 $h = 190$ m (North) and $h = 225$ m (South) and for Polar 6 $h = 250$ m (both positions).

agreement of all turbulent quantities obtained from both aircraft shows that the results are reliable enough to see the differences between the ABL structures of 5 June, 14 June and 20 June. Turbulence decreased to almost zero at about $z = 0.7h$. This is roughly where the capping inversion started. Although no Nevzorov data was available for this flight, visual observations suggested that the cloud layer reached far into this capping inversion. This phenomenon was much more pronounced than on

5   14 March, when probably the surface forced and cloud forced convection led to a well-mixed ABL.

To understand the differences between the results from both flight days with multi-layer clouds, it is also important to mention that the absolute values of wind speeds did not differ much from each other on both days. Thus differences between the days are most probably caused by the different density stratifications. The stability observed on 20 June caused strongly reduced values of σ_w^2 (also of σ_u^2 and σ_v^2, not shown for 20 June) relative to the data on 14 June and consequently, also the

10   TKE was much lower on 20 June. Variances and TKE decreased to zero at cloud top, which is not really the case on 14 June.

This comparison shows for both flight days an impressing agreement between the measurements of both nosebooms installed at two aircraft. This holds especially for the results of 20 June, when the signals from both nosebooms were very low, but nevertheless, very close to each other. Obviously, the situation was horizontally also very homogeneous, note that the maximum distance between legs was almost 150 km.

15   **4   Discussion**

We have shown that cloud top radiative cooling strongly affects the turbulent structure of the ABL. In the following, we will consider in some more detail its consequences for the turbulent processes in case of the single layer cloud on 5 June 2017. The presented data (Fig. 5) showed that the rapid increase of the turbulent heat flux across the upper part of the cloud layer amounted to about 15 W m^{-2} (Fig. 5a). This is much smaller than the 50-70 W m^{-2} jump of the net terrestrial radiative energy

20   flux based on Fig. 4. The question arises what magnitude of the turbulent heat flux maximum in the cloud layer we can expect if we assume that turbulence redistributes the observed terrestrial radiative cooling through the mixed layer. In the following, we investigate this issue using a diagnostic mixed-layer model with data from slanted profiles.

Mixed-layer models of different complexity have been used extensively to study various aspects of the stratocumulus-topped mixed layers (e.g. Lilly, 1968; Nicholls, 1984; Turton and Nicholls, 1987; Stevens, 2002). Here, a simple mixed-layer model

25   (described in Appendix B) is used to reconstruct the vertical profile of turbulent heat flux using the observed profile of the net terrestrial radiative energy flux LW_{net}. The key assumption is that the total flux of a conservative variable changes linearly with height in order to provide a uniform cooling or heating of a mixed layer. Here, the liquid-water potential temperature θ_l and the total water mixing ratio q_t are used as conservative variables.

Also, the convective mixed-layer scaling is typically used in many turbulence closures. Therefore, it is important to quantify

30   the velocity and temperature scales based on our observations. In the original mixed-layer scaling, the surface buoyancy flux and the mixed-layer depth h are applied to obtain the velocity and temperature scales. In a cloud-topped ABL, it is more appropriate to use the integral I of the vertical turbulent buoyancy flux (Deardorff, 1980; Nicholls, 1989). Thereby, the generalized

Table 1. The characteristics of the observed profiles on the 5 June 2017.

Profile	h_{top} (m)	h_{cb} (m)	$\Delta\theta_{top}$ (K)	Δq_v (g/kg)	ΔLW_{net} (Wm^{-2})	LWP (gm^{-2})	w_* (ms^{-1})	θ_* (K)
T1	420	90	2.8	0.4	75	72	0.41	0.017
T2	540	320	5.4	0.6	60	20	0.59	0.023
T3	525	300	4.9	0.5	58	21	0.45	0.014
T4	480	240	4.8	0.5	56	44	0.42	0.014
T5	500	300	4.8	-0.17	61	–	0.47	0.016
PS	420	170	4.5	0.45	63	30	0.50	0.022

convective velocity and temperature scales are

$$w_* = (2.5I)^{1/3}, \tag{9}$$
$$\theta_* = w_*^2\theta_v/gh, \tag{10}$$

where

$$5 \quad I = (g/\theta_0) \int_{h_{bot}}^{h_{top}} \overline{w'\theta'_v}\,dz, \tag{11}$$

where h_{bot} and h_{top} are the heights of the mixed-layer bottom and top, respectively. Unfortunately, the vertical flux of the virtual potential temperature $\overline{w'\theta'_v}$ was not measured. However, $\overline{w'\theta'_v}$ is very close to the potential temperature flux $\overline{w'\theta'}$ at low temperatures due to the low amount of moisture and small moisture flux. Thus, in Eq. (11) we use $\overline{w'\theta'}$ instead of $\overline{w'\theta'_v}$.

We summarize the characteristics of the profiles in Table 1 and include the convective scales w_* and θ_* which are calculated

10 using the observed heat flux.

In order to use the mixed-layer model, it is necessary to determine the bottom height of the mixed layer h_{bot} where the observed fluxes could be prescribed. In many profiles the heat flux was close to zero at about 90 m height, which was below the cloud base. Thus we set $h_{bot} = 90$ m where both $\overline{w'\theta'_l}$ and $\overline{w'q'_t}$ are set to zero, as we expect moisture flux to be also negligibly small in the absence of a strong surface forcing. The values of $\overline{w'\theta'_l}$ and $\overline{w'q'_t}$ at the cloud top are parameterized as described in

15 Appendix B.

The diagnosed turbulent heat flux is shown in Figure 5a. Clearly, the mixed-layer model is producing positive heat flux in the cloud layer with a maximum located in its upper part (near $z = 0.8h$). The modelled value of the entrainment heat flux parameterized using (B11) and (B13) is in close agreement with the observed one. However, the observed heat flux in the layer $0.7\,h < z < 0.9\,h$ is significantly smaller than the diagnosed one so that the observed maximum is at at a lower level

20 ($z = 0.6\,h$). Thus, the values of w_* and θ_*, 0.66 ms^{-1} and 0.04 K, respectively, obtained using the diagnosed heat flux are larger than those based on the observed fluxes.

Nearly all slanted profiles showed increased vertical velocity variance in the cloud (Figure 5d). The maximum values of $\overline{w'^2}$ were in the range between 0.2 and about 0.35 ms^{-1}. These result in the ratio $\sigma_{w,max}/w_* \approx 1.0$, which is larger than the reported values of 0.6-0.65 for stratocumulus in midlatitudes (Nicholls, 1984; Caughey et al., 1982; Deardorff, 1980). However, using the value $w_* = 0.66$ ms^{-1}, which is based on the heat-flux profile diagnosed by the mixed-layer model, results in $\sigma_{w,max}/w_* \approx 0.7$. The latter is closer to the reported values.

Lenschow et al. (1980) suggested the following parameterization for σ_w/w_*, namely

$$\frac{\sigma_w^2}{w_*^2} = 1.8 \left[\frac{z_{top} - z}{z_{top} - z_{bot}} \right]^{2/3} \left[1 - 0.8 \frac{z_{top} - z}{z_{top} - z_{bot}} \right]^2 , \qquad (12)$$

where z_{top} and z_{bot} are the mixed-layer top and bottom heights, respectively. Equation (12) is valid for $z_{bot} \leq z < z_{top}$. Figure 5d shows σ_w derived from the parametrization(12) if $w_* = 0.66$ is used as diagnosed by the mixed-layer model. Obviously, (12) is in good agreement with the observations when $w_* = 0.66$ ms^{-1} is used. Using the w_* values based on the observed heat flux would result in an underestimation of σ_w^2. This suggests that the strength of the observed turbulence in terms of σ_w^2 would require for its generation a larger heat flux than the observed one. However, one should keep in mind the simplicity of the mixed layer model assuming, e.g. horizontal homogeneity in the ABL. It confirms at least roughly the magnitude of the observed heat flux and shows that a heat flux of 25 W m^{-2} would be enough to redistribute the observed terrestrial radiative cooling.

5 Conclusions

We presented and analyzed airborne measurements of turbulence and radiation obtained during the campaign ACLOUD over the marginal sea ice zone to the north and northwest of Svalbard. By combining two types of flight patterns we obtained vertical profiles of turbulent quantities on the basis of the eddy covariance method. The first approach was the classical one, in which we derived turbulence statistics from horizontal flights at approximately constant heights. This method provided the most precise quantitative estimates of turbulence statistics, however, the vertical resolution of the obtained profiles was limited to only several points in the ABL. The second method, not often applied by others so far, delivered turbulence statistics from slanted ascents or descents. This resulted in vertically higher resolved profiles of turbulence statistics but with higher statistical uncertainty. Nevertheless, we demonstrated a satisfying agreement of turbulence statistics obtained from the two different approaches based on different types of flight patterns. Also, the vertical structures of the derived profiles of turbulence quantities do not contradict each other and can be explained physically. This gives additional confidence into the data that is beyond the statistical evaluation of the accuracy at just one height level.

The presented analysis of the vertical turbulence profiles attempts to distinguish the effect of clouds on turbulence statistics in comparison to the role of other mechanisms of turbulence generation. We showed that the cloud-top terrestrial radiative cooling is forcing upside-down convection, which shapes the ABL turbulent structure, especially in its upper part and during weak synoptic wind. In situations with only one cloud layer, the cloud impact is identified by local maxima of the vertical

velocity variance and heat flux in the cloud layer, as well as by a negative vertical velocity skewness. In this respect, an Arctic stratocumulus-topped ABL is similar to other cloud-topped ABLs in lower latitudes despite its shallowness and lower humidity.

We showed that strong cloud-top cooling causes the third moments $T_{SH} = \overline{w'^2\theta'}$ and $T_{TV} = \overline{w'\theta'^2}$ to be negative in the cloud layer hinting at the possible importance of nonlocal transport associated with large eddies. However, this is only a hint

5 and quantifying the role of the third-order transport has to be a subject of a separate study. Here, we did not analyze the second-order moment budgets and thus cannot conclude on the relative role of various processes, as was done for a cloud-topped ABL in the LES-based study by Heinze et al. (2015).

Stronger synoptic wind and shallowness of the ABL resulted in shear-generated turbulence playing a more important role in shaping the ABL turbulent structure than the cloud impact. This statement holds true even in the presence of strong cloud-top

10 cooling. Namely, the strong-wind case that has been investigated was characterized by a pronounced maximum of the variance of all three velocity components and TKE located at low altitude in the subcloud layer.

When mid-level clouds were present, the cloud-top cooling in the lower cloud layer located in the ABL became essentially weaker. This resulted in a much weaker turbulence in the ABL even despite stronger wind. In such conditions, the ABL stability associated with surface-air temperature difference and wind speed apparently becomes an important factor influencing the ABL

15 turbulence. This concerns both turbulence magnitude and the ABL turbulent structure.

To conclude, our results suggest that cloud-top cooling is one of the major sources of turbulence in the spring-summer Arctic ABL even despite its typical shallowness and relative dryness. We found that the amount of such cooling strongly depends on the presence of mid-level clouds, as concluded earlier also by other studies based on radar observations. The importance for the ABL structure depends among other factors mainly on wind speed, ABL height, and stability.

20 Thus for an adequate representation of the ABL turbulence in coarse-resolution models a tight coupling between the radiative, microphysical, and turbulence parameterizations is needed. The presented cases may serve as a reference for further studies focusing on the evaluation of such parameterizations.

We stress that the number of cases, which we considered, was limited and the results should motivate for future research. However, we have shown by the few cases that there is large complexity due to the many forcing parameters but a detailed

25 consideration helps to understand the mechanisms. Moreover, an understanding of these processes is relevant for the polar climate due to the strong impact on the energy fluxes. Future measurements would be helpful to further study the described phenomena.

Data availability. The 1Hz-averaged noseboom data is available in Hartmann et al. (2019a). The full-resolution noseboom data at 100Hz is available in Hartmann et al. (2019b). The 1Hz-averaged liquid and total water content from the Nevzorov data is available in Chechin (2019).

30 The vertical profiles of the net terrestrial radiation are available in Stapf et al. (2019). MODIS images are avaliable at https://ladsweb.modaps.eosdis.nasa.go ERA5 reanalysis data is available at https://climate.copernicus.eu/.
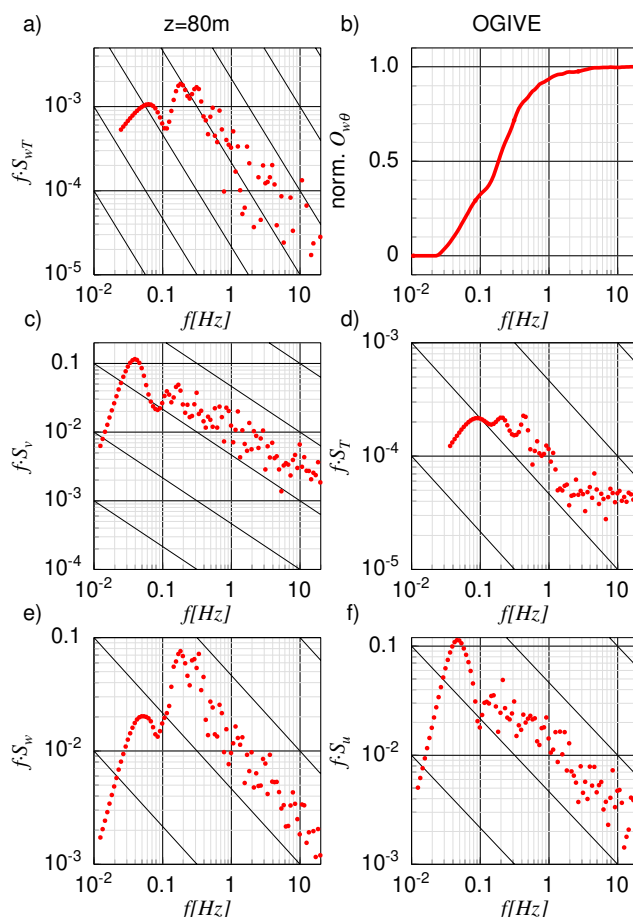
Figure A1. Frequency weighted power spectra and ogive $O_{w,\theta}$ at 80 m height, as measured on 5 June 2017 below the cloud.

Appendix A: Accuracy

Before ACLOUD the Polar 5 and 6 turbulence equipment was never used inside clouds and especially not in clouds above sea ice where the cloud generated turbulence is small but dominating. Such conditions are challenging because, e.g. heat fluxes are mostly much smaller than in strong convective conditions over the open ocean (see airborne measurements described by Gryanik and Hartmann (2002)) or over leads described in earlier applications of the used turbulence probe by Tetzlaff et al. (2015). Thus the accuracy of the measurements needs to be reconsidered. Apart from instrumentation characteristics, other
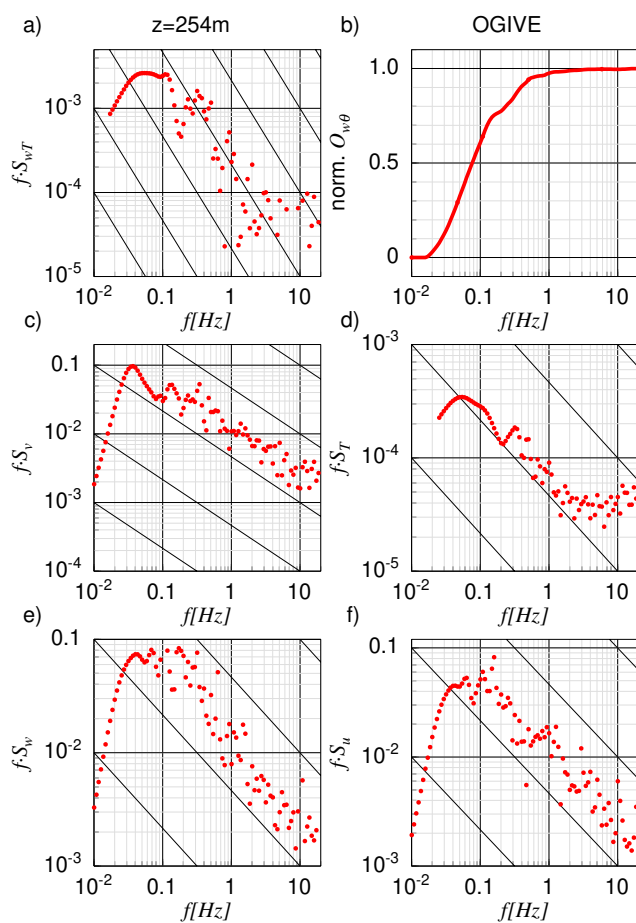
Figure A2. As Figure A1 but measurements have been obtained in the cloud at 254 m height.
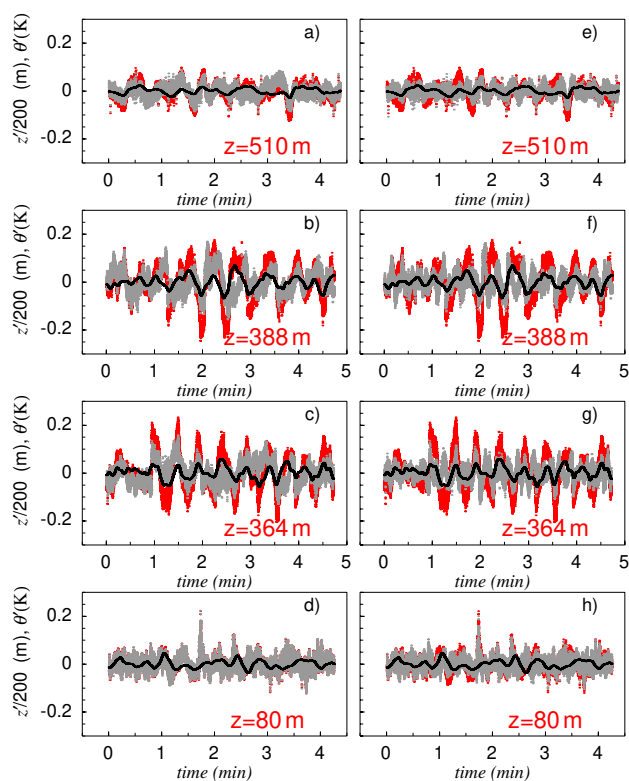
Figure A3. Deviation of potential temperature θ (red) and height (black solid lines) from leg averages as a function of time. (red: uncorrected, grey: height dependence of θ corrected by the vertical temperature gradient (panels a-d) and by applying a highpass filter at 0.05 Hz) (panels e-h) as described in the text). Results from four legs flown at different heights above the surface are shown. The lowermost one was below the cloud, the uppermost one was above the cloud and other ones within the cloud.
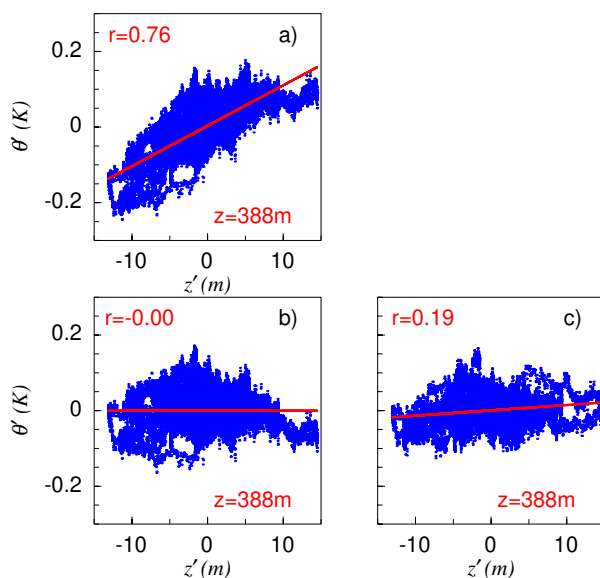
Figure A4. θ deviation from mean value as a function of height deviation for 5 June 2017 without correction (top) and with correction (bottom) (left: subtraction of vertical gradient of θ; right: high pass filtered at 0.05 Hz).
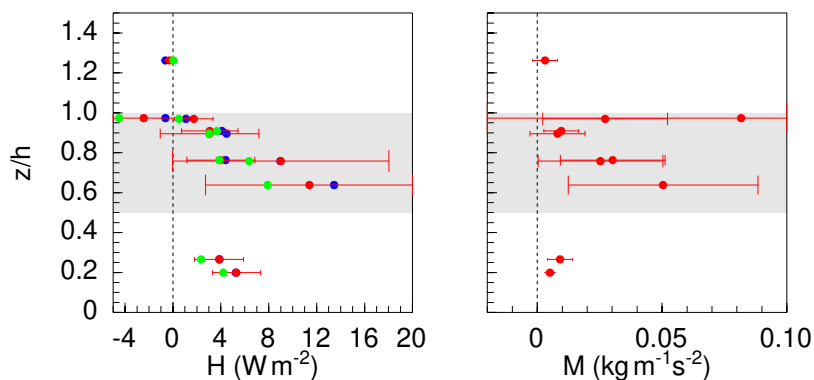
Figure A5. Left panel: Fluxes of sensible heat as measured on 5 June 2017, height corrected with method 1 (red), method 2 (black), and uncorrected (blue).Right panel: Momentum flux as measured on 5 June 2017. Whiskers in both panels show the sampling error ϵ determined following Friehe et al. (1991)

factors are influencing the accuracy as described in Section 2.2. The accuracy of the turbulence measurements in clouds will be considered in the following for the typical case of 5 June 2017.

On this day, eight horizontal flight legs have been flown, one clearly below the cloud layer, five legs within the cloud and another two sections above the cloud. Cloud base and cloud top have been observed at 200 m and 400 m, respectively.

5   Frequency weighted power spectra for three wind components, potential temperature and heat flux are shown in Figures A1 and A2 as an example for the leg flown below the cloud (Figure A1) and within the cloud (Figure A2). Spectra of u, v, and w show the characteristic slope of -2/3 (corresponding to -5/3 without weighting) in the inertial subrange over more than two orders of magnitude. Similarly, heat flux multiplied with the frequency shows the required -4/3 slope. Temperature variations at high frequencies (above 5 Hz) become very small and reach the detection limit. Thus the temperature variance spectra begin to

10   exhibit some white noise beyond 5 Hz. However, this has no serious impact on the measured heat flux, which becomes obvious by considering ogives $O_{w,\theta}$ representing the cumulative integration of the cospectrum $Co_{w,\theta}$ between the highest and lowest measured frequency (Friehe et al., 1991). Based on the ogives shown in Figures A1 and A2 one can conclude that at least 95 % of the fluxes are caused by contributions below 1 Hz. Maxima for w and θ are between 0.1 Hz and 0.2 Hz dependent on the aircraft height. This corresponds to wave lengths of about 1.5-3.5 km, when we assume an average aircraft speed of 55 ms^{-1}.

15   The ogive shows some deviation from an ideal S-shape at the low frequency (large wave length) end of the spectrum. This might point to a too short leg length, however, a prolongation would have led to other difficulties since usually, homogeneity of turbulence is not guaranteed over larger distances than the 10-18 km during our measurements because of inhomogeneities in the cloud structures.

Another difficulty arises however, especially in the upper part of the cloud and especially in the capping inversion and regions

20   with strong increase of potential temperature with height. There, we found a correlation between the height of the aircraft and the temperature as can be seen in Figures A3 and A4. We tested two different strategies to filter this dependency. The first (method 1) was to correct the temperature series for the turbulence analysis based on the mean measured vertical temperature gradient along the flight leg. The second (method 2) was to apply a band pass filter to remove the frequency related to the oscillation of the aircraft height from all time series. Results from all methods are shown in Figures A3 and A4. The advantage

25   of method 1 is that the correlation goes to zero after correction, but there is still a remaining local dependence. With method 2 the correlation is also reduced, however, one cannot exclude that also a physical contribution is filtered. We show the effect of both methods in Figure A5. It shows that the impact of this correction is in the range of the sampling error ϵ (shown here for the results obtained with method 1). ϵ was determined as in Friehe et al. (1991) dependent on the leg length and flight altitude above ground. Figure A5 also shows the momentum flux M with the corresponding ϵ.

30   We need to address, however, also some uncertainty of air temperature observations in clouds caused by evaporation of liquid from the sensing element (Lenschow and Pennell, 1974) and of droplets during the adiabatic heating of air in the housing of the sensor (Lemone, 1980; Albrecht et al., 1979). We have to leave an experimental determination of this error for future research for the used Rosemount temperature sensor and can only speculate that the related error for turbulence is probably not too large in the cold Arctic conditions with relatively low absolute humidity. With respect to the accuracy of the temperature

35   measurements it is a good sign at least that results of both aircraft agree well when flight legs have been flown close to each

other (see Ehrlich et al. (2019)) within a thin cloud at a distance of about 200 m. At such a distance one can expect that both temperature sensors have not been exposed to the same humidity conditions so that a possible error due to evaporation effects might have caused differences in the temperatures.

Also, in Sections 3 and 4 we show that all vertical profiles can be physically well explained. This concerns both the profiles
5 derived from horizontal flight legs and those from the slanted profile flights. Concerning the latter, we need to assume that the statistical error is probably larger as compared with the horizontal legs, so that especially those results need to be considered with some caution. Nevertheless, results are at least reasonable. It is also important to see that profiles of different turbulence moments do not show contrasting results. This gives additional confidence in the data that is beyond the pure statistical evaluation and should also be kept in mind when the accuracy is considered.

10 **Appendix B: Diagnostic mixed-layer model**

We choose the following variables that are approximately conservative during the moist-adiabatic processes in the mixed-layer: the liquid-water potential temperature θ_l and the total liquid water mixing ratio q_t. The latter two are defined as

$$\theta_l = \theta - \left(\frac{\theta}{T}\right)\frac{L}{c_p}q_c , \tag{B1}$$

$$q_t = q_v + q_c , \tag{B2}$$

15 where L is the heat of vaporization, c_p is specific heat at constant pressure, q_c is the liquid water content and q_v is specific humidity. Below the cloud base, i.e. for $z < h_{cb}$ we have simply $\theta_l = \theta$ and $q_t = q_v$ as shown in Fig. B1.

As follows from the mixed-layer assumption, the total vertical fluxes of the conserved variables are linear functions of z for $h_b \geq z \geq h_t$, where $h_{b,t}$ are the bottom- and top heights of the mixed-layer. Namely, one obtains

$$\overline{w'\theta_l'} + LW_{net} = \frac{z - h_b}{h_t - h_b}(\overline{w'\theta_l'} + LW_{net})\big|_{z=h_t} + \frac{h_t - z}{h_t - h_b}(\overline{w'\theta_l'} + LW_{net})\big|_{z=h_b} , \tag{B3}$$

20 $$\overline{w'q_t'} = \frac{z - h_b}{h_t - h_b}(\overline{w'q_t'})\big|_{z=h_t} + \frac{h_t - z}{h_t - h_b}(\overline{w'q_t'})\big|_{z=h_b} . \tag{B4}$$

The above equations allow one to diagnose the profiles of $\overline{w'\theta_l'}$ from the observed profiles of LW_{net}. However, we are more interested in diagnosing the vertical profiles of $\overline{w'\theta'}$ which can then be directly compared to the observed ones. Such diagnostic relations for $\overline{w'\theta'}$ are given further following Deardorff (1976a).

Following the definition of θ_l, in the cloud layer, the turbulent flux $\overline{w'\theta'}$ is

25 $$\overline{w'\theta'} = \overline{w'\theta_l'} + \frac{\theta}{T}\frac{L}{c_p}\overline{w'q_c'} . \tag{B5}$$

In saturated air

$$\overline{w'q_v'} = \overline{w'q_s'} = \frac{L}{R_v T\theta}q_s\overline{w'\theta'} , \tag{B6}$$
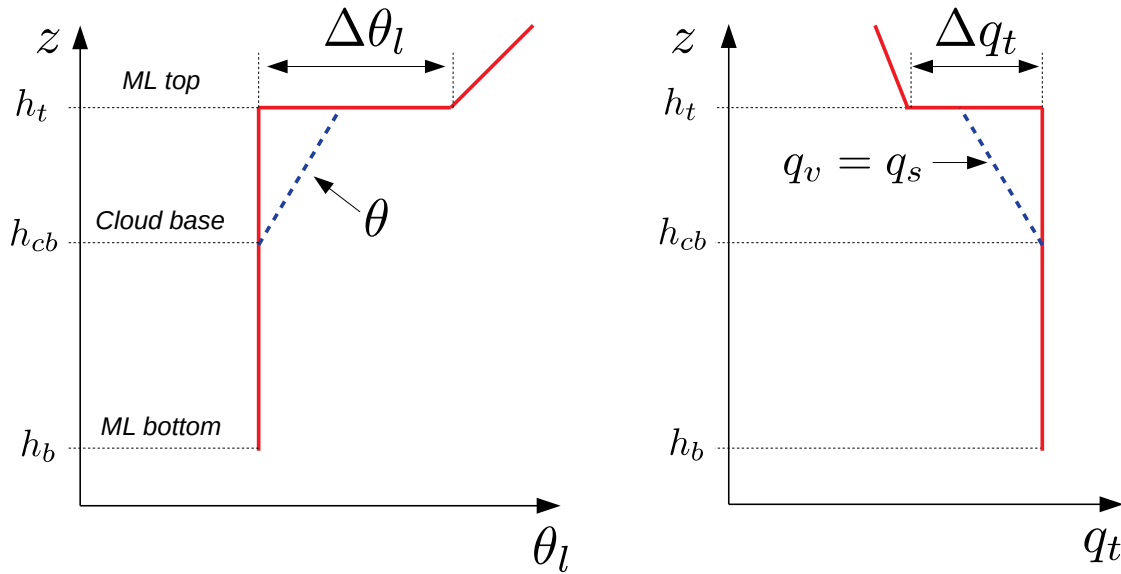
Figure B1. Schematic representation of the vertical profiles of the conserved variables θ_l and q_t in the mixed layer.

where q_s is saturation specific humidity and R_v is the gas constant for water vapor. Since $\overline{w'q'_c} = \overline{w'q'_t} - \overline{w'q'_v}$ we can rewrite (B5) as

$$\overline{w'\theta'} = \left[\overline{w'\theta'_l} + \left(\frac{\theta}{T} \frac{L}{c_p} \overline{w'q'_t} \right) \right] \left[1 + \frac{L^2}{c_p R_v T^2} q_s \right]^{-1} . \tag{B7}$$

Below the cloud base we simply have $\overline{w'\theta'} = \overline{w'\theta'_l}$.

5   It is also useful to obtain a diagnostic relation for the virtual potential temperature flux $\overline{w'\theta'_v}$ which is associated with the buoyancy flux. If we neglect the small contribution of the liquid cloud water q_c to air density, the virtual potential flux is

$$\overline{w'\theta'_v} = \overline{w'\theta'} + \theta \left(1 + 0.61 \overline{w'q'_v} \right) . \tag{B8}$$

In the cloud layer we can use (B6) in (B8) to obtain

$$\overline{w'\theta'_v} = \overline{w'\theta'} \left[1 + 0.61 q_s \left(1 + \frac{L}{R_v T} \right) \right] , \tag{B9}$$

10   while below the cloud layer

$$\overline{w'\theta'_v} = \overline{w'\theta'_l} + \theta \left(1 + 0.61 \overline{w'q'_t} \right) . \tag{B10}$$

The turbulent entrainment fluxes $\overline{w'\theta_l'}\big|_{z=h_t}$ and $\overline{w'q_t'}\big|_{z=h_t}$ across the boundary-layer top are parameterized as

$$\overline{w'\theta_l'}\big|_{z=h_t} = -w_e\Delta\theta_l \, , \tag{B11}$$

$$\overline{w'q_t'}\big|_{z=h_t} = -w_e\Delta q_t \, , \tag{B12}$$

where $\Delta\theta_l = \Delta\theta - L/c_p\Delta q_c$ and $\Delta q_t = \Delta q_v + \Delta q_c$ are the jumps of the conservative variables across the mixed-layer top. For the entrainment velocity, we use one of the most simple parameterizations, namely

$$w_e = A\frac{\theta_0}{g}\frac{w_*^3}{\Delta\theta_v\Delta h} \, , \tag{B13}$$

where $A = 0.2$ is the typically used value of the proportionality constant. In (B13), we assume $\Delta\theta_v \approx \Delta\theta$.

Thus, similar to Randall (1980) we assume that all of the observed radiative flux divergence occurs in the turbulent cloudy layer. This results in that the whole amount of radiative cooling forces buoyancy-driven production of turbulence within the mixed layer, which, in turn, leads to entrainment. It should be noted that another approach exists (e.g., Deardorff, 1976b, 1981) according to which a fraction of radiative cooling occurs already in the inversion layer. This happens when Reynolds or spatial averaging is considered and applied to the observations or to the results of large-eddy simulations. Due to an undulations of the cloud top this leads to an existence of a smoothed transition layer where both turbulent cloud tops and non-turbulent clear air occur.

Author contributions. DC, CL, AE and MW concenptualized the study and worked out the methodology. All of the authors took part in the ACLOUD campaign in 2017 to obtain the observational data used in the study. JH carried out the initial data processing and the five-hole probe calibration. DC and CL processed the data to obtain turbulence statistics and carried out the analysis of the obtained results. DC formulated and applied the mixed-layer model.

Competing interests. None of the authors have any competing interests

Acknowledgements. We gratefully acknowledge the funding of the German Research Foundation DFG, Deutsche Forschungsgemeinschaft) of the Transregional Collaborative Research Center SFB/TRR 172 (Project-ID 268020496). Part of the analysis of the turbulence statistics by D. Chechin was funded by the Russian Science Foundation grant 18-77-10072-P and data processing by D. Chechin was funded by Russian Ministry of Science and Higher Education, agreement No. 075-15-2019-1621. DC thanks Johannes Stapf for processing observations of radiative fluxes, for the initial script for plotting MODIS images as well as for fruitful discussions.

References

Albrecht, B. A., Cox, S. K., and Schubert, W. H.: Radiometric measurements of in-cloud temperature fluctuations, Journal of Applied Meteorology and Climatology, 18, 1066–1071, 1979.

Aliabadi, A. A., Staebler, R. M., Liu, M., and Herber, A.: Characterization and Parametrization of Reynolds Stress and Turbulent Heat Flux in the Stably-Stratified Lower Arctic Troposphere Using Aircraft Measurements, Boundary-Layer Meteorology, 161, 99–126, https://doi.org/10.1007/s10546-016-0164-7, https://doi.org/10.1007/s10546-016-0164-7, 2016.

Brooks, I. M., Tjernström, M., Persson, P. O. G., Shupe, M. D., Atkinson, R. A., Canut, G., Birch, C. E., Mauritsen, T., Sedlar, J., and Brooks, B. J.: The Turbulent Structure of the Arctic Summer Boundary Layer During The Arctic Summer Cloud-Ocean Study, Journal of Geophysical Research: Atmospheres, 122, 9685–9704, https://doi.org/https://doi.org/10.1002/2017JD027234, https://agupubs.onlinelibrary.wiley.com/doi/abs/10.1002/2017JD027234, 2017.

Caughey, S. J., Crease, B. A., and Roach, W. T.: A field study of nocturnal stratocumulus II Turbulence structure and entrainment, Quarterly Journal of the Royal Meteorological Society, 108, 125–144, https://doi.org/https://doi.org/10.1002/qj.49710845508, https://rmets.onlinelibrary.wiley.com/doi/abs/10.1002/qj.49710845508, 1982.

Chechin, D.: Liquid water content measured by the Nevzorov probe during the aircraft ACLOUD campaign in the Arctic, https://doi.org/10.1594/PANGAEA.906658, https://doi.org/10.1594/PANGAEA.906658, 2019.

Chechin, D. G. and Lüpkes, C.: Boundary-Layer Development and Low-level Baroclinicity during High-Latitude Cold-Air Outbreaks: A Simple Model, Boundary-Layer Meteorology, 162, 91–116, https://doi.org/10.1007/s10546-016-0193-2, https://doi.org/10.1007/s10546-016-0193-2, 2017.

Chechin, D. G., Lüpkes, C., Repina, I. A., and Gryanik, V. M.: Idealized dry quasi 2-D mesoscale simulations of cold-air outbreaks over the marginal sea ice zone with fine and coarse resolution, Journal of Geophysical Research: Atmospheres, 118, 8787–8813, 2013.

Clark, J. P., Shenoy, V., Feldstein, S. B., Lee, S., and Goss, M.: The Role of Horizontal Temperature Advection in Arctic Amplification, Journal of Climate, 34, 2957 – 2976, https://doi.org/10.1175/JCLI-D-19-0937.1, https://journals.ametsoc.org/view/journals/clim/34/8/JCLI-D-19-0937.1.xml, 2021.

Curry, J., Hobbs, P., King, M., Randall, D., Minnis, P., Isaac, G., Pinto, J., Uttal, T., Bucholtz, A., Cripe, D., et al.: FIRE Arctic clouds experiment, Bulletin of the American Meteorological Society, 81, 5–30, 2000.

Curry, J. A., Ebert, E. E., and Herman, G. F.: Mean and turbulence structure of the summertime Arctic cloudy boundary layer, Quarterly Journal of the Royal Meteorological Society, 114, 715–746, https://doi.org/https://doi.org/10.1002/qj.49711448109, https://rmets.onlinelibrary.wiley.com/doi/abs/10.1002/qj.49711448109, 1988.

Curry, J. A., Schramm, J. L., Rossow, W. B., and Randall, D.: Overview of Arctic Cloud and Radiation Characteristics, Journal of Climate, 9, 1731–1764, https://doi.org/10.1175/1520-0442(1996)009<1731:OOACAR>2.0.CO;2, https://doi.org/10.1175/1520-0442(1996)009<1731:OOACAR>2.0.CO;2, 1996.

Dahlke, S. and Maturilli, M.: Contribution of Atmospheric Advection to the Amplified Winter Warming in the Arctic North Atlantic Region, Advances in Meteorology, 2017, 4928 620, https://doi.org/10.1155/2017/4928620, https://doi.org/10.1155/2017/4928620, 2017.

Deardorff, J. W.: Usefulness of Liquid-Water Potential Temperature in a Shallow-Cloud Model, Journal of Applied Meteorology, 15, 98–102, https://doi.org/10.1175/1520-0450(1976)015<0098:UOLWPT>2.0.CO;2, https://doi.org/10.1175/1520-0450(1976)015<0098:UOLWPT>2.0.CO;2, 1976a.

Deardorff, J. W.: On the entrainment rate of a stratocumulus-topped mixed layer, Quarterly Journal of the Royal Meteorological Society, 102, 563–582, https://doi.org/https://doi.org/10.1002/qj.49710243306, https://rmets.onlinelibrary.wiley.com/doi/abs/10.1002/qj.49710243306, 1976b.

Deardorff, J. W.: Stratocumulus-capped mixed layers derived from a three-dimensional model, Boundary-Layer Meteorology, 18, 495–527, 1980.

Deardorff, J. W.: On the distribution of mean radiative cooling at the top of a stratocumulus-capped mixed layer, Quarterly Journal of the Royal Meteorological Society, 107, 191–202, https://doi.org/https://doi.org/10.1002/qj.49710745112, https://rmets.onlinelibrary.wiley.com/doi/abs/10.1002/qj.49710745112, 1981.

Egerer, U., Gottschalk, M., Siebert, H., Ehrlich, A., and Wendisch, M.: The new BELUGA setup for collocated turbulence and radiation measurements using a tethered balloon: first applications in the cloudy Arctic boundary layer, Atmospheric Measurement Techniques, 12, 4019–4038, https://doi.org/10.5194/amt-12-4019-2019, https://www.atmos-meas-tech.net/12/4019/2019/, 2019.

Egerer, U., Ehrlich, A., Gottschalk, M., Griesche, H., Neggers, R. A., Siebert, H., and Wendisch, M.: Case study of a humidity layer above Arctic stratocumulus and potential turbulent coupling with the cloud top, Atmospheric Chemistry and Physics, 21, 6347–6364, 2021.

Ehrlich, A., Wendisch, M., Lüpkes, C., Buschmann, M., Bozem, H., Chechin, D., Clemen, H.-C., Dupuy, R., Eppers, O., Hartmann, J., et al.: A comprehensive in situ and remote sensing data set from the Arctic CLoud Observations Using airborne measurements during polar Day (ACLOUD) campaign, Earth System Science Data, 11, 1853–1881, 2019.

Finger, J. E. and Wendling, P.: Turbulence structure of Arctic stratus clouds derived from measurements and calculations, Journal of Atmospheric Sciences, 47, 1351–1373, 1990.

Friehe, C., Shaw, W., Rogers, D., Davidson, K., Large, W., Stage, S., Crescenti, G., Khalsa, S., Greenhut, G., and Li, F.: Air-sea fluxes and surface layer turbulence around a sea surface temperature front, Journal of Geophysical Research: Oceans, 96, 8593–8609, 1991.

Goosse, H., Kay, J. E., Armour, K. C., Bodas-Salcedo, A., Chepfer, H., Docquier, D., Jonko, A., Kushner, P. J., Lecomte, O., Massonnet, F., et al.: Quantifying climate feedbacks in polar regions, Nature communications, 9, 1–13, 2018.

Graversen, R. G., Mauritsen, T., Tjernström, M., Källén, E., and Svensson, G.: Vertical structure of recent Arctic warming, Nature, 451, 53–56, 2008.

Gryanik, V. M. and Hartmann, J.: A Turbulence Closure for the Convective Boundary Layer Based on a Two-Scale Mass-Flux Approach, Journal of the Atmospheric Sciences, 59, 2729 – 2744, https://doi.org/10.1175/1520-0469(2002)059<2729:ATCFTC>2.0.CO;2, https://journals.ametsoc.org/view/journals/atsc/59/18/1520-0469_2002_059_2729_atcftc_2.0.co_2.xml, 2002.

Hartmann, J., Gehrmann, M., Kohnert, K., Metzger, S., and Sachs, T.: New calibration procedures for airborne turbulence measurements and accuracy of the methane fluxes during the AirMeth campaigns, Atmospheric Measurement Techniques, 11, 4567–4581, https://doi.org/10.5194/amt-11-4567-2018, https://www.atmos-meas-tech.net/11/4567/2018/, 2018.

Hartmann, J., Lüpkes, C., and Chechin, D.: 1Hz resolution aircraft measurements of wind and temperature during the ACLOUD campaign in 2017, https://doi.org/10.1594/PANGAEA.902849, https://doi.org/10.1594/PANGAEA.902849, 2019a.

Hartmann, J., Lüpkes, C., and Chechin, D.: High resolution aircraft measurements of wind and temperature during the ACLOUD campaign in 2017, https://doi.org/10.1594/PANGAEA.900880, https://doi.org/10.1594/PANGAEA.900880, 2019b.

Heinze, R., Mironov, D., and Raasch, S.: Second-moment budgets in cloud topped boundary layers: A large-eddy simulation study, Journal of Advances in Modeling Earth Systems, 7, 510–536, 2015.

Hersbach, H., Bell, B., Berrisford, P., Hirahara, S., Horányi, A., Muñoz-Sabater, J., Nicolas, J., Peubey, C., Radu, R., Schepers, D., et al.: The ERA5 global reanalysis, Quarterly Journal of the Royal Meteorological Society, 146, 1999–2049, 2020.

Hogan, R. J., Grant, A. L., Illingworth, A. J., Pearson, G. N., and O'Connor, E. J.: Vertical velocity variance and skewness in clear and cloud-topped boundary layers as revealed by Doppler lidar, Quarterly Journal of the Royal Meteorological Society: A journal of the atmospheric sciences, applied meteorology and physical oceanography, 135, 635–643, 2009.

Intrieri, J. M., Fairall, C. W., Shupe, M. D., Persson, P. O. G., Andreas, E. L., Guest, P. S., and Moritz, R. E.: An annual cycle of Arctic surface cloud forcing at SHEBA, Journal of Geophysical Research: Oceans, 107, SHE 13–1–SHE 13–14, https://doi.org/https://doi.org/10.1029/2000JC000439, 2002.

Knudsen, E. M., Heinold, B., Dahlke, S., Bozem, H., Crewell, S., Gorodetskaya, I. V., Heygster, G., Kunkel, D., Maturilli, M., Mech, M., Viceto, C., Rinke, A., Schmithüsen, H., Ehrlich, A., Macke, A., Lüpkes, C., and Wendisch, M.: Meteorological conditions during the ACLOUD/PASCAL field campaign near Svalbard in early summer 2017, Atmospheric Chemistry and Physics, 18, 17 995–18 022, https://doi.org/10.5194/acp-18-17995-2018, https://www.atmos-chem-phys.net/18/17995/2018/, 2018.

Korolev, A. V., Strapp, J. W., Isaac, G. A., and Nevzorov, A. N.: The Nevzorov Airborne Hot-Wire LWC–TWC Probe: Principle of Operation and Performance Characteristics, Journal of Atmospheric and Oceanic Technology, 15, 1495–1510, https://doi.org/10.1175/1520-0426(1998)015<1495:TNAHWL>2.0.CO;2, https://doi.org/10.1175/1520-0426(1998)015<1495:TNAHWL>2.0.CO;2, 1998.

Lemone, M. A.: On the difficulty of measuring temperature and humidity in cloud: Comments on "Shallow convection on day 261 of GATE: Mesoscale arcs", Monthly Weather Review, 108, 1702–1705, 1980.

Lenschow, D., Wyngaard, J. C., and Pennell, W. T.: Mean-field and second-moment budgets in a baroclinic, convective boundary layer, Journal of Atmospheric Sciences, 37, 1313–1326, 1980.

Lenschow, D., Society, A. M., and for Atmospheric Research (U.S.), N. C.: Probing the atmospheric boundary layer, American Meteorological Society, https://books.google.de/books?id=EC9RAAAAMAAJ, 1986.

Lenschow, D. H. and Pennell, W. T.: On the Measurement of In-Cloud and Wet-Bulb Temperatures from an Aircraft, Monthly Weather Review, 102, 447 – 454, https://doi.org/10.1175/1520-0493(1974)102<0447:OTMOIC>2.0.CO;2, https://journals.ametsoc.org/view/journals/mwre/102/6/1520-0493_1974_102_0447_otmoic_2_0_co_2.xml, 1974.

Lenschow, D. H., Li, X. S., Zhu, C. J., and Stankov, B. B.: The stably stratified boundary layer over the great plains, Boundary-Layer Meteorology, 42, 95–121, https://doi.org/10.1007/BF00119877, https://doi.org/10.1007/BF00119877, 1988.

Lilly, D. K.: Models of cloud-topped mixed layers under a strong inversion, Quarterly Journal of the Royal Meteorological Society, 94, 292–309, 1968.

Mahrt, L.: Vertical Structure and Turbulence in the Very Stable Boundary Layer, Journal of Atmospheric Sciences, 42, 2333 – 2349, https://doi.org/10.1175/1520-0469(1985)042<2333:VSATIT>2.0.CO;2, https://journals.ametsoc.org/view/journals/atsc/42/22/1520-0469_1985_042_2333_vsatit_2_0_co_2.xml, 1985.

McFarquhar, G. M., Ghan, S., Verlinde, J., Korolev, A., Strapp, J. W., Schmid, B., Tomlinson, J. M., Wolde, M., Brooks, S. D., Cziczo, D., et al.: Indirect and semi-direct aerosol campaign: The impact of Arctic aerosols on clouds, Bulletin of the American Meteorological Society, 92, 183–201, 2011.

Moeng, C.-H.: Large-eddy simulation of a stratus-topped boundary layer. Part I: Structure and budgets, Journal of the atmospheric sciences, 43, 2886–2900, 1986.

Morrison, H., de Boer, G., Feingold, G., Harrington, J., Shupe, M. D., and Sulia, K.: Resilience of persistent Arctic mixed-phase clouds, Nature Geoscience, 5, 11, https://doi.org/10.1038/ngeo1332, 2011.

Morrison, H., de Boer, G., Feingold, G., Harrington, J., Shupe, M. D., and Sulia, K.: Resilience of persistent Arctic mixed-phase clouds, Nature Geoscience, 5, 11–17, https://doi.org/10.1038/ngeo1332, https://doi.org/10.1038/ngeo1332, 2012.

Nicholls, S.: The dynamics of stratocumulus: Aircraft observations and comparisons with a mixed layer model, Quarterly Journal of the Royal Meteorological Society, 110, 783–820, 1984.

Nicholls, S.: The structure of radiatively driven convection in stratocumulus, Quarterly Journal of the Royal Meteorological Society, 115, 487–511, 1989.

5   Osborne, E., Richter-Menge, J., and Jeffries, M.: Arctic report card 2018, Washington, DC: National Park Service, 2018.

Overland, J. E., Wood, K. R., and Wang, M.: Warm Arctič2014cold continents: climate impacts of the newly open Arctic Sea, Polar Research, 30, 15 787, 2011.

Pithan, F. and Mauritsen, T.: Arctic amplification dominated by temperature feedbacks in contemporary climate models, Nature Geoscience, 7, 181–184, https://doi.org/10.1038/ngeo2071, https://doi.org/10.1038/ngeo2071, 2014.

10   Pithan, F., Medeiros, B., and Mauritsen, T.: Mixed-phase clouds cause climate model biases in Arctic wintertime temperature inversions, Climate Dynamics, 43, 289–303, 2014.

Pithan, F., Svensson, G., Caballero, R., Chechin, D., Cronin, T. W., Ekman, A. M. L., Neggers, R., Shupe, M. D., Solomon, A., Tjernström, M., and Wendisch, M.: Role of air-mass transformations in exchange between the Arctic and mid-latitudes, Nature Geoscience, 11, 805–812, https://doi.org/10.1038/s41561-018-0234-1, https://doi.org/10.1038/s41561-018-0234-1, 2018.

15   Randall, D. A.: Entrainment into a Stratocumulus Layer with Distributed Radiative Cooling, Journal of Atmospheric Sciences, 37, 148 – 159, https://doi.org/10.1175/1520-0469(1980)037<0148:EIASLW>2.0.CO;2, https://journals.ametsoc.org/view/journals/atsc/37/1/1520-0469_1980_037_0148_eiaslw_2_0_co_2.xml, 1980.

Roesler, E. L., Posselt, D. J., and Rood, R. B.: Using large eddy simulations to reveal the size, strength, and phase of updraft and downdraft cores of an Arctic mixed-phase stratocumulus cloud, Journal of Geophysical Research: Atmospheres, 122, 4378–4400,

20   https://doi.org/https://doi.org/10.1002/2016JD026055, https://agupubs.onlinelibrary.wiley.com/doi/abs/10.1002/2016JD026055, 2017.

Sedlar, J. and Shupe, M. D.: Characteristic nature of vertical motions observed in Arctic mixed-phase stratocumulus, Atmospheric Chemistry and Physics, 14, 3461–3478, https://doi.org/10.5194/acp-14-3461-2014, https://www.atmos-chem-phys.net/14/3461/2014/, 2014.

Serreze, M. C. and Francis, J. A.: The Arctic amplification debate, Climatic change, 76, 241–264, 2006.

Shupe, M. D., Walden, V. P., Eloranta, E., Uttal, T., Campbell, J. R., Starkweather, S. M., and Shiobara, M.: Clouds at Arctic Atmo-

25   spheric Observatories. Part I: Occurrence and Macrophysical Properties, Journal of Applied Meteorology and Climatology, 50, 626–644, https://doi.org/10.1175/2010JAMC2467.1, https://doi.org/10.1175/2010JAMC2467.1, 2011.

Shupe, M. D., Persson, P. O. G., Brooks, I. M., Tjernström, M., Sedlar, J., Mauritsen, T., Sjogren, S., and Leck, C.: Cloud and boundary layer interactions over the Arctic sea ice in late summer, Atmospheric Chemistry and Physics, 13, 9379–9399, https://doi.org/10.5194/acp-13-9379-2013, https://www.atmos-chem-phys.net/13/9379/2013/, 2013.

30   Solomon, A., Shupe, M. D., Persson, P. O. G., and Morrison, H.: Moisture and dynamical interactions maintaining decoupled Arctic mixed-phase stratocumulus in the presence of a humidity inversion, Atmospheric Chemistry and Physics, 11, 10 127–10 148, https://doi.org/10.5194/acp-11-10127-2011, https://acp.copernicus.org/articles/11/10127/2011/, 2011.

Solomon, A., Shupe, M. D., Persson, O., Morrison, H., Yamaguchi, T., Caldwell, P. M., and de Boer, G.: The sensitivity of springtime Arctic mixed-phase stratocumulus clouds to surface-layer and cloud-top inversion-layer moisture sources, Journal of the Atmospheric Sciences,

35   71, 574–595, 2014.

Sotiropoulou, G., Sedlar, J., Tjernström, M., Shupe, M. D., Brooks, I. M., and Persson, P. O. G.: The thermodynamic structure of summer Arctic stratocumulus and the dynamic coupling to the surface, Atmospheric Chemistry and Physics, 14, 12 573–12 592, https://doi.org/10.5194/acp-14-12573-2014, https://www.atmos-chem-phys.net/14/12573/2014/, 2014.

Stapf, J., Ehrlich, A., Jäkel, E., and Wendisch, M.: Cloud radiative forcing, LWP and cloud-free albedo derived from airborne broadband irradiance observations during the ACLOUD campaign, https://doi.org/10.1594/PANGAEA.909289, https://doi.org/10.1594/PANGAEA.909289, 2019.

Stapf, J., Ehrlich, A., Jäkel, E., Lüpkes, C., and Wendisch, M.: Reassessment of shortwave surface cloud radiative forcing in the Arctic: consideration of surface-albedo–cloud interactions, Atmospheric Chemistry and Physics, 20, 9895–9914, 2020.

Stevens, B.: Entrainment in stratocumulus-topped mixed layers, Quarterly Journal of the Royal Meteorological Society: A journal of the atmospheric sciences, applied meteorology and physical oceanography, 128, 2663–2690, 2002.

Tetzlaff, A., Lüpkes, C., and Hartmann, J.: Aircraft-based observations of atmospheric boundary-layer modification over Arctic leads, Quarterly Journal of the Royal Meteorological Society, 141, 2839–2856, https://doi.org/https://doi.org/10.1002/qj.2568, https://rmets. onlinelibrary.wiley.com/doi/abs/10.1002/qj.2568, 2015.

Tjernström, M.: Turbulence Length Scales in Stably Stratified Free Shear Flow Analyzed from Slant Aircraft Profiles, Journal of Applied Meteorology and Climatology, 32, 948 – 963, https://doi.org/10.1175/1520-0450(1993)032<0948:TLSISS>2.0.CO;2, https://journals. ametsoc.org/view/journals/apme/32/5/1520-0450_1993_032_0948_tlsiss_2_0_co_2.xml, 1993.

Tjernström, M., Žagar, M., Svensson, G., Cassano, J. J., Pfeifer, S., Rinke, A., Wyser, K., Dethloff, K., Jones, C., Semmler, T., and Shaw, M.: 'Modelling the Arctic Boundary Layer: An Evaluation of Six Arcmip Regional-Scale Models using Data from the Sheba Project', Boundary-Layer Meteorology, 117, 337–381, https://doi.org/10.1007/s10546-004-7954-z, https://doi.org/10.1007/s10546-004-7954-z, 2005.

Tjernström, M., Sedlar, J., and Shupe, M. D.: How well do regional climate models reproduce radiation and clouds in the Arctic? An evaluation of ARCMIP simulations, Journal of Applied Meteorology and Climatology, 47, 2405–2422, 2008.

Tjernström, M., Leck, C., Birch, C. E., Bottenheim, J. W., Brooks, B. J., Brooks, I. M., Bäcklin, L., Chang, R. Y.-W., de Leeuw, G., Di Liberto, L., de la Rosa, S., Granath, E., Graus, M., Hansel, A., Heintzenberg, J., Held, A., Hind, A., Johnston, P., Knulst, J., Martin, M., Matrai, P. A., Mauritsen, T., Müller, M., Norris, S. J., Orellana, M. V., Orsini, D. A., Paatero, J., Persson, P. O. G., Gao, Q., Rauschenberg, C., Ristovski, Z., Sedlar, J., Shupe, M. D., Sierau, B., Sirevaag, A., Sjogren, S., Stetzer, O., Swietlicki, E., Szczodrak, M., Vaattovaara, P., Wahlberg, N., Westberg, M., and Wheeler, C. R.: The Arctic Summer Cloud Ocean Study (ASCOS): overview and experimental design, Atmospheric Chemistry and Physics, 14, 2823–2869, https://doi.org/10.5194/acp-14-2823-2014, https://www.atmos-chem-phys.net/14/ 2823/2014/, 2014.

Turton, J. and Nicholls, S.: A study of the diurnal variation of stratocumulus using a multiple mixed layer model, Quarterly Journal of the Royal Meteorological Society, 113, 969–1009, 1987.

Uttal, T., Curry, J. A., McPhee, M. G., Perovich, D. K., Moritz, R. E., Maslanik, J. A., Guest, P. S., Stern, H. L., Moore, J. A., Turenne, R., et al.: Surface heat budget of the Arctic Ocean, Bulletin of the American Meteorological Society, 83, 255–276, 2002.

Verlinde, J., Harrington, J. Y., McFarquhar, G., Yannuzzi, V., Avramov, A., Greenberg, S., Johnson, N., Zhang, G., Poellot, M., Mather, J. H., et al.: The mixed-phase Arctic cloud experiment, Bulletin of the American Meteorological Society, 88, 205–222, 2007.

Wendisch, M., Brückner, M., Burrows, J., Crewell, S., Dethloff, K., Ebell, K., Lüpkes, C., Macke, A., Notholt, J., Quaas, J., et al.: ArctiC amplification: climate relevant atmospheric and SurfaCe processes, and feedback mechanisms:(AC) 3, Eos, Trans. Amer. Geophys. Union, 98, 2017.

Wendisch, M., Macke, A., Ehrlich, A., Lüpkes, C., Mech, M., Chechin, D., Dethloff, K., Velasco, C. B., Bozem, H., Brückner, M., Clemen, H.-C., Crewell, S., Donth, T., Dupuy, R., Ebell, K., Egerer, U., Engelmann, R., Engler, C., Eppers, O., Gehrmann, M., Gong, X., Gottschalk, M., Gourbeyre, C., Griesche, H., Hartmann, J., Hartmann, M., Heinold, B., Herber, A., Herrmann, H., Heygster, G., Hoor, P.,

Jafariserajehlou, S., Jäkel, E., Järvinen, E., Jourdan, O., Kästner, U., Kecorius, S., Knudsen, E. M., Köllner, F., Kretzschmar, J., Lelli, L., Leroy, D., Maturilli, M., Mei, L., Mertes, S., Mioche, G., Neuber, R., Nicolaus, M., Nomokonova, T., Notholt, J., Palm, M., van Pinxteren, M., Quaas, J., Richter, P., Ruiz-Donoso, E., Schäfer, M., Schmieder, K., Schnaiter, M., Schneider, J., Schwarzenböck, A., Seifert, P., Shupe, M. D., Siebert, H., Spreen, G., Stapf, J., Stratmann, F., Vogl, T., Welti, A., Wex, H., Wiedensohler, A., Zanatta, M., and Zeppenfeld, S.: The Arctic Cloud Puzzle: Using ACLOUD/PASCAL Multiplatform Observations to Unravel the Role of Clouds and Aerosol Particles in Arctic Amplification, Bulletin of the American Meteorological Society, 100, 841–871, https://doi.org/10.1175/BAMS-D-18-0072.1, https://doi.org/10.1175/BAMS-D-18-0072.1, 2019.

Wesche, C., Steimhage, D., and Nixdorf, U.: Polar aircraft Polar 5 and POlar6 operated by the Alfred Wegener Institute. J. Large-Scale Res. Facil., 2, A87, 2016.

Young, G. S.: Turbulence structure of the convective boundary layer. Part I. Variability of normalized turbulence statistics, Journal of Atmospheric Sciences, 45, 719–726, 1988.

Zilitinkevich, S., Gryanik, V. M., Lykossov, V. N., and Mironov, D. V.: Third-Order Transport and Nonlocal Turbulence Closures for Convective Boundary Layers, Journal of the Atmospheric Sciences, 56, 3463 – 3477, https://doi.org/10.1175/1520-0469(1999)056<3463:TOTANT>2.0.CO;2, https://journals.ametsoc.org/view/journals/atsc/56/19/1520-0469_1999_056_3463_totant_2.0.co_2.xml, 1999.